Doctoral Dissertation

Tracking atmospheric chemical components in accordance with the Sustainable Development Goals (SDGs)

Phan Anh

November 16, 2023

Graduate School of Engineering
Chubu University

A Doctoral Dissertation
submitted to Graduate School of Engineering,
Chubu University
in partial fulfillment of the requirements for the degree of
Doctor of ENGINEERING

Phan Anh

Thesis Committee:

Professor Hiromichi Fukui	(Supervisor)
Professor Kiyoshi Honda	(Chubu University)
Professor Jun Izutsu	(Chubu University)
Professor Masao Takano	(Nagoya University)

Tracking atmospheric chemical components in accordance with the Sustainable Development Goals (SDGs)*

Phan Anh

Abstract

Lorem ipsum dolor sit amet, consectetur adipisicing elit, sed do eiusmod tempor incididunt ut labore et dolore magna aliqua. Ut enim ad minim veniam, quis nostrud exercitation ullamco laboris nisi ut aliquip ex ea commodo consequat. Duis aute irure dolor in reprehenderit in voluptate velit esse cillum dolore eu fugiat nulla pariatur. Excepteur sint occaecat cupidatat non proident, sunt in culpa qui officia deserunt mollit anim id est laborum.

Lorem ipsum dolor sit amet, consectetur adipisicing elit, sed do eiusmod tempor incididunt ut labore et dolore magna aliqua. Ut enim ad minim veniam, quis nostrud exercitation ullamco laboris nisi ut aliquip ex ea commodo consequat. Duis aute irure dolor in reprehenderit in voluptate velit esse cillum dolore eu fugiat nulla pariatur. Excepteur sint occaecat cupidatat non proident, sunt in culpa qui officia deserunt mollit anim id est laborum.

Keywords:

π, astronomy, mathematics, computer, algorithm

---

*Doctoral Dissertation, Graduate School of Information Science, Nara Institute of Science and Technology, November 16, 2023.

Contents

List of Figures

List of Tables

1 Introduction

1.1 Background

2 Background

2.1 Air pollution

2.2 Greenhouse gas

Lorem ipsum dolor sit amet, consectetur adipisicing elit, sed do eiusmod tempor incididunt ut labore et dolore magna aliqua. Ut enim ad minim veniam, quis nostrud exercitation ullamco laboris nisi ut aliquip ex ea commodo consequat. Duis aute irure dolor in reprehenderit in voluptate velit esse cillum dolore eu fugiat nulla pariatur. Excepteur sint occaecat cupidatat non proident, sunt in culpa qui officia deserunt mollit anim id est laborum.

AIR POLLUTIOM INDUCED BY INTERVENTION EVENTS

3 Ukraine's case study

3.1 Introduction

Nitrogen dioxide (NO_2) is a key air pollutant that can have harmful effects on human health. An increase in nitrogen oxide (NOx = NO + NO2) concentrations contributes to global warming through a chemical reaction that leads to the formation of ozone (O3), a short- lived climate pollutant with a potent warming effect (Stocker et al., 2013). The lifetime of NO2 is strongly influenced by photochemical reactions and meteorological parameters (Barré et al., 2021) and varies seasonally (Dragomir et al., 2015; Kendrick et al., 2015). During winter, photochemical reaction activity is reduced, resulting in a longer lifetime of the NO2. Additionally, seasonal variations in NO2 concentration are controlled by dispersion processes which are significantly affected by changes in boundary layer height (BLH), wind speed and direction patterns due to temperature inversions in summer and winter (Barré et al., 2021; Kendrick et al., 2015). NO2 concentration levels have been widely used to evaluate decreases in emissions associated with intervention events such as the COVID-19 pandemic lockdown and impacts on the air quality due to the short lifetime of NO2 in the atmosphere (Barré et al., 2021; Cooper et al., 2022). In Europe, anthropogenic NOx emissions are mainly attributed to combustion processes in transportation, as well as energy production and distribution.

In Ukraine, coal-fired power plants (CPPs) dominantly account for 80% of total SO2 and 25% of total NOx emissions, and some have been identified as the highest-emitting CPPs in the region and in the world (Lauri and Rosa, 2021). Since the pandemic started in March 2020, and now with the ongoing armed conflict with Russia, Ukraine has faced a series of threats to the economy, human security and the environment, as well as geopolitical tensions (Pereira et al., 2022). During the pandemic response starting in 2020, many national and local lockdown restrictions were issued to prevent the spread of the virus, causing a sharp decrease in gross domestic product growth rate, as well as industrial and energy production (Danylyshyn, 2020). In 2021, Ukraine's economy started to recover from the pandemic but the recovery was eventually upended by an armed conflict with Russia that started on February 24, 2022. The conflict has been causing a multi-pronged crisis not only in Ukraine but also in Europe, with increased prices and exacerbated inflation among the many impacts. Many facilities and extensive areas of housing and other infrastructure, including some CPPs, have been reported destroyed or damaged in Ukraine. These impacts have consequently triggered an unprecedented refugee crisis in Ukraine, clogging border crossings between Ukraine and bordering European countries (Júlia et al., 2022). The many socio-economic changes that have occurred during the pandemic and the conflict could be expected to contribute to major variability in air quality in Ukraine, including NO2 pollution levels, during the 2020–2022 period.

A report by the United Nations Development Programme (UNDP) (Dumitru et al., 2020), estimated the impacts of the pandemic lockdown on NO2 levels in Ukraine by using Sentinel 5P (S5P) NO2 column concentrations and Copernicus Atmosphere Monitoring Service (CAMS) surface NO2 data (Marécal et al., 2015). However, meteorological variables were not acknowledged, although ignoring weather factors could strongly affect final estimates of changes in pollution concentration levels induced by the lockdown (Schiermeier, 2020). A more recent study (Zalakeviciute et al., 2022) utilized direct satellite observation from 2019 and early 2020 as business-as-usual data to evaluate the impact of the Russia-Ukraine conflict in 2022 on air quality, but again, without acknowledging weather effects. These two studies utilized estimates of year-to-year differences. However, such estimates can easily be affected and dominated by changes in meteorological parameters rather than emission sources (Grange et al., 2021; Shi et al., 2021). Therefore, a more sophisticated method is needed to measure the impacts of intervention events through better quantification of actual air quality.

In order to normalize the meteorological effects to accurately and reliably quantify the impact of intervention events, the use of machine learning is increasingly being adopted, but mostly applied for ground-based measurements following the original idea proposed by (Grange et al., 2018) and (Grange and Carslaw, 2019). The objective of this approach is to construct a business-as-usual (BAU) model for predicting air pollution levels independently of the impacts of any intervention events. This is achieved by integrating meteorological, spatial, and temporal features into the model during the BAU period to accurately represent air pollution levels. An intervention event, in this context, refers to an occurrence that has caused changes in air quality. Recently, (Barré et al., 2021) have introduced their weather normalization approach to improve estimates of lockdown impacts not only on NO2 levels from ground-based observations and CAMS simulations, but also in satellite measurements from S5P. The original method in (Grange et al., 2018; Grange and Carslaw, 2019) has been altered in order to work with satellite retrieval column NO2 concentration levels from S5P by adopting a new feature, the forecast surface NO2 level from CAMS data. Alternatively, gradient boosting machines (GBMs) (Friedman, 2001) have been also utilized instead of random forests (Grange et al., 2018) to develop weather-normalization models under the BAU conditions. (Barré et al., 2021) reported an overall reduction (ranging from 23% to 32%) in major European cities using the three datasets. Their study showed an average difference of 14% between satellite-based and ground-based estimates, and 11% between simulations from the CAMS regional ensemble of air quality models and ground-based estimates. These findings suggest that estimates of the impacts of the lockdown on NO2 levels can vary depending on the source of the data.

This chapter aims to investigate the actual satellite-derived column NO2 pollution levels induced by pandemic lockdown restrictions and the armed conflict with Russia, which have been two major changes in human activities in Ukraine since 2019. In order to do so, we developed a weather-normalization model under BAU scenarios for S5P column NO2 levels to decouple the meteorological effects from the intervention effects. The BAU simulation NO2 levels are then used to quantify changes in S5P column NO2 concentrations during the lockdown and the armed conflict. We describe the data used in the study in section 3.2 and the methodology in section 3.3. The results and discussion on NO2 level changes are summarized in section 3.4 for the lockdown, and section 3.5 for the armed conflict. Finally, we conclude the results of the study in section 3.6.

3.2 Data

3.2.1 Selection of analysis periods

In this study, we consider the three years 2019, 2020, and 2022 for our analysis. We assumed that in 2019, before the lockdown in 2020 and the armed conflict with Russia in 2022, there were no other significant factors impacting socio-economic activities. Hence, we used 2019 NO2 pollution levels as the reference data for development of the BAU model.

Ukraine reported its first active case of COVID-19 on March 3, 2020, and began closing its borders to foreign citizens from March 15 onwards. Around the same time, the country also witnessed its first COVID-19 related death. On April 6, the government introduced a strict lockdown, imposing significant restrictions on movement and requiring the public to wear masks in public spaces. This lockdown was eventually extended until June, although certain restrictions were already lifted starting from May 11. For the lockdown component of our study, we focused on two specific periods: the pre-lockdown period, which ran from March 1 to 15, 2020, and the strict lockdown period, spanning from April 6 to May 10, 2020. The decision to count the pre-lockdown period from March 1 was based on the lack of qualified S5P data available for analysis before March, as indicated in 3.2. In 2021, even though COVID-19 vaccines had been developed and distributed to citizens of Ukraine (vaccinations started on February 24, 2021), many local lockdowns and restrictions continued to be issued to cope with growing numbers of daily COVID-19 active cases, while trying to keep socio-economic activities on track for recovery.

The Russia-Ukraine conflict began on February 24, 2022. We employed data for the period February 1 to July 31 each year from 2019 to 2022 for NO2 variability analysis. This time frame covers the pre-lockdown and lockdown periods in 2020 and extends beyond the first five months (February 24 to July 31) of the armed conflict in 2022.

3.2.2 TROPOMI NO2 from Sentinel 5P

Most previous studies assessing the impacts of intervention involved ground observations in their analysis. However, reliable ground measurement data was only available in Kyiv (capital of Ukraine) as other sites had been damaged or destroyed in the armed conflict and taken out of service (Savenets, 2021). Thus, open satellite data is considered the most efficient way to monitor air quality for all parts of Ukrainian territory (Shelestov et al., 2021).

The S5P data has been distributed from 2018 to the present with two available options. The first is original data (ORG) processed with either of two versions of processor, v1.x (5/2018–6/2021) or v2.x (7/2021 onwards). The second is reprocessed datasets (RPRO) with the processor (v2.x) for the full mission. According to (Van Geffen et al., 2022), the S5P NO2 v2.2 data has larger vertical column density (VCDs) than v1.x data, ranging from 10% to 40%, mostly found at mid and high latitudes in winter. Therefore, bias between S5P v1.x and v2.x could lead to overestimation and underestimation when comparing air pollution data in 2022 versus 2019, thereby affecting evaluations of the conflict's impacts on S5P NO2 levels.

In this study, we conducted experiments using two versions of S5P NO2 data. The first dataset is ORG data which was collected through level 3 (L3) offline processing (OFF) of the S5P product available on Google Earth Engine (Gorelick et al., 2017). This dataset comprises processed data from different processor versions for each year from 2019 to 2022 (v1.3.1 in 2019, v1.3.2 in 2020, and v2.3.1 in 2022). The second dataset, denoted as the RPRO product, employs processor version v2.4.0 for the full mission duration. This dataset was acquired from the Sentinel-5P Pre-Operations Data Hub (s5phub.copernicus.eu) using the Sentinelsat API.

Regarding the RPRO data, we began by downloading the level 2 (L2) dataset. In order to generate the L3 NO2 dataset, each operational L2 product underwent mosaicking and filtering of low-quality pixels, which involved removing items with quality assurance (QA) values less than 75% for the "tropospheric_NO2_column_number_density" band. The harpconvert tool was utilized to perform the conversion from L2 to L3 product. Subsequently, both datasets were linearly interpolated to a spatial resolution of 0.1×0.1 degree. At

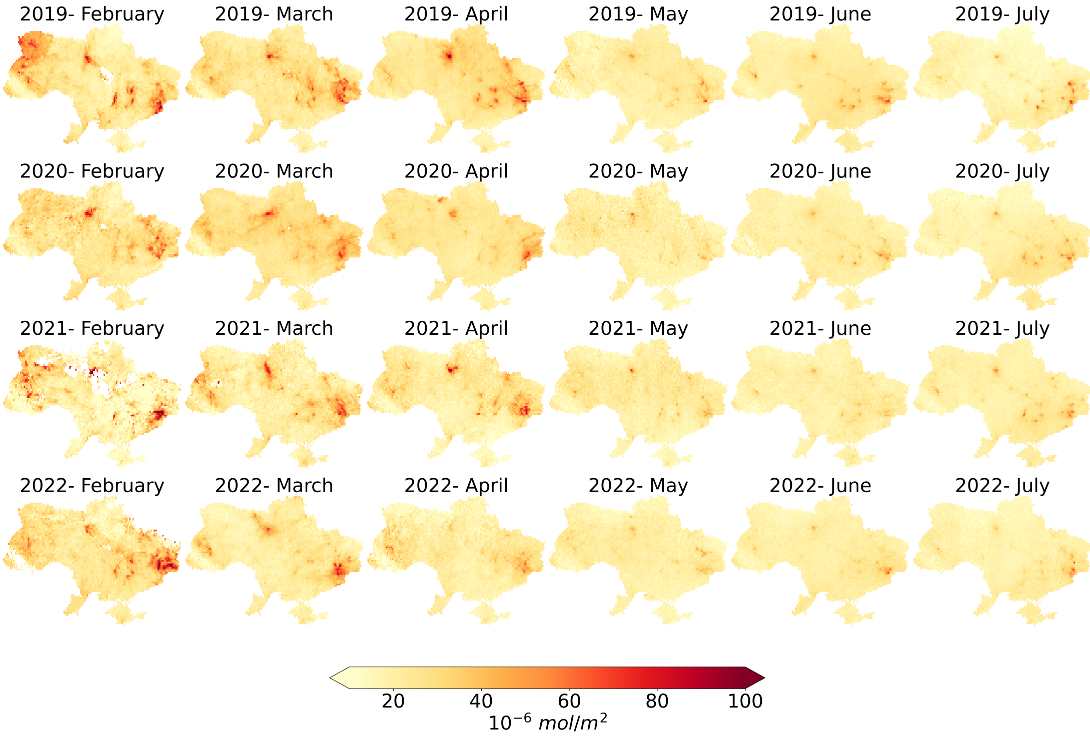

(a) ORG data

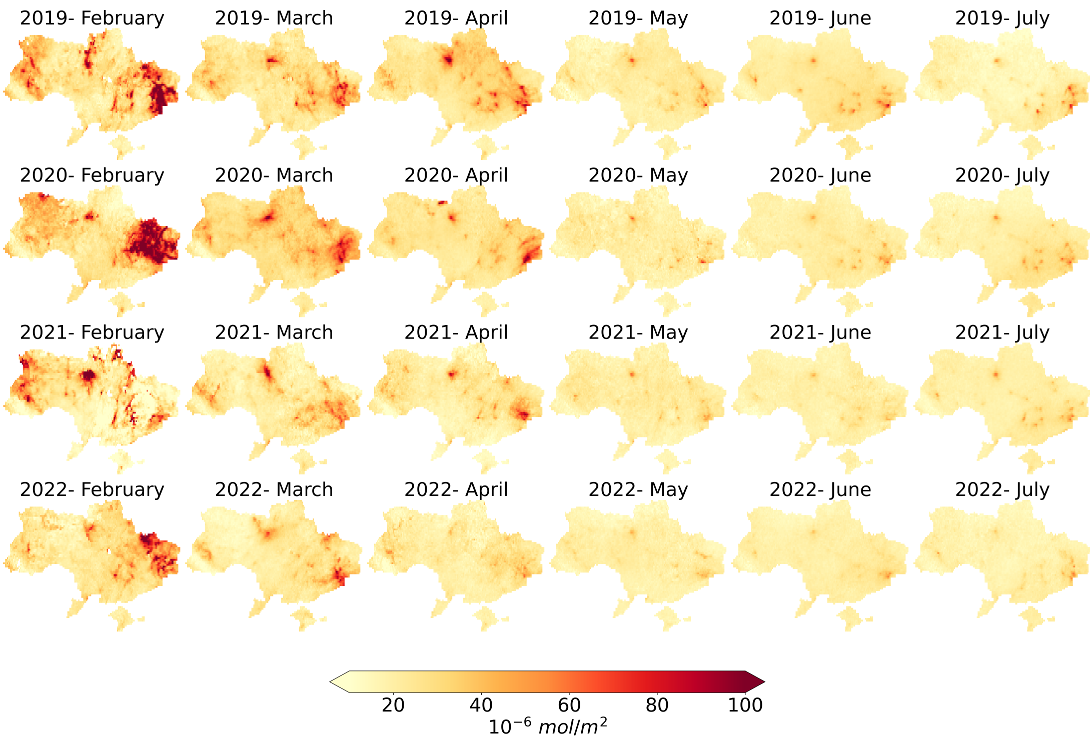

(b) RPRO data

Figure 3.1. Monthly (February to July) average map of TROPOMI S5P NO2 tropospheric columns for Ukraine from 2019 to 2022

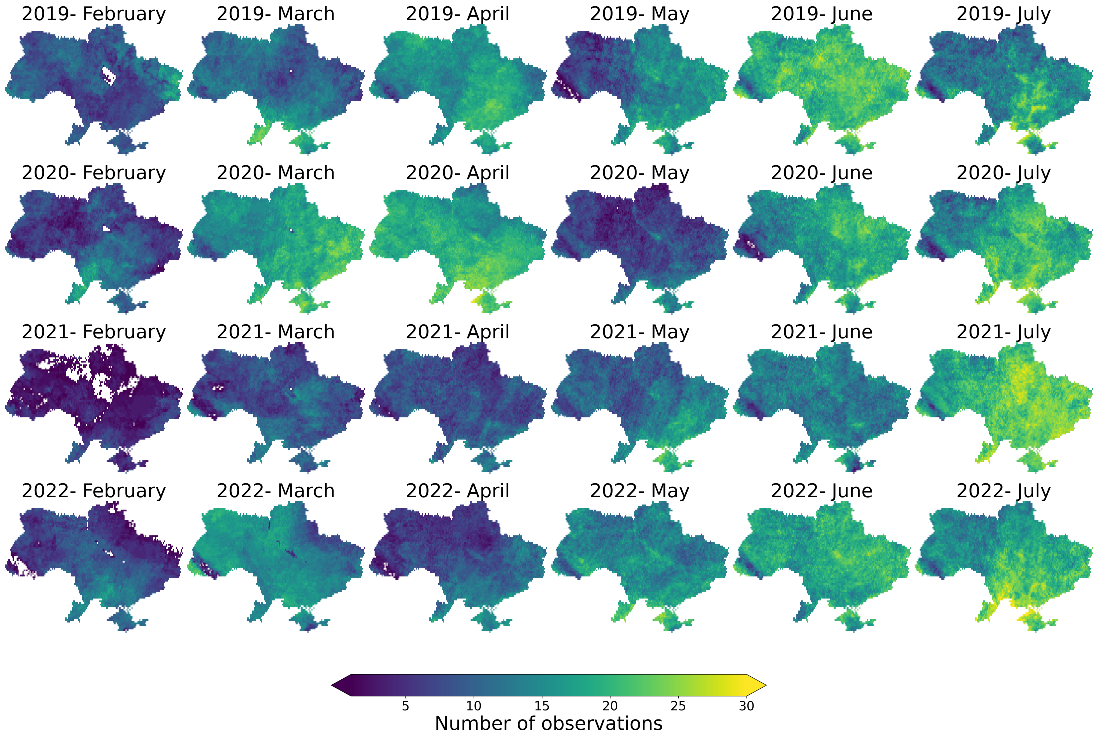

(a) ORG data

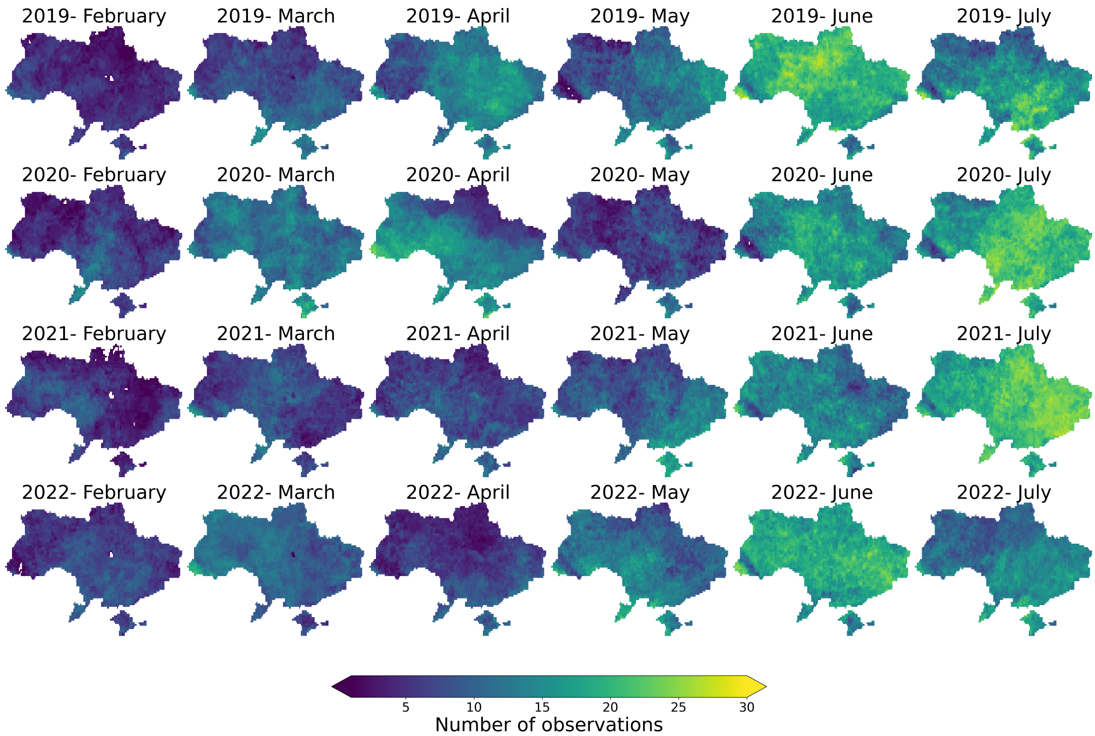

(b) RPRO data

Figure 3.2. Monthly (from February to July) number of TROPOMI S5P NO2 tropospheric columns observations for Ukraine from 2019 to 2022

the time of the experiment, the RPRO data was only accessible until July 2022.

Plots presented in Figure 3.1 display the average monthly TROPOMI NO2 tropospheric column over Ukraine from 2019 to 2022 (February to July) using the ORG data (Figure 3.1a) and RPRO data (Figure 3.1b), respectively. In 2020, a reduction of 4.8% (ORG data) and 8.3% (RPRO data) in mean NO2 levels over the Ukrainian territory was observed from April to May, compared to levels recorded in 2019. In 2022, a reduction of 2.4% (ORG data) and 2.9% (RPRO data) was seen from March to July, compared to levels recorded in 2021. Additionally, during the same period, a reduction of 10.3% (ORG data) and 15% (RPRO data) was observed, compared to the NO2 levels recorded in 2019. We observed that the reduction in NO2 levels was more significant in the RPRO data compared to the ORG data, both during the lockdown in 2020 and the first five months (March–July) of the conflict in 2022 in Ukraine.

We summarize the number of qualified observations available for each month from 2019 to 2022 (February to July) in Ukraine using the ORG data (Figure 3.2a) and RPRO data (Figure 3.2b). The quantification of seasonal NO2 levels can be challenging, particularly during the selected months in winter (February) and spring (March, April) of 2021 and 2022, due to the limited availability of qualified observations. This is further complicated when attempting to estimate changes before and after intervention events such as the lockdown and the armed conflict in Ukraine, as the before period falls within the winter months when observations are scarce.

3.2.3 Meteorological and surface NO2 data

In this study, the meteorological and surface NO2 data are utilized as the predictors for the estimation of NO2 under BAU conditions as suggested by (Barré et al., 2021). The meteorological data is ERA5 reanalysis data which is collected from the Climate Data Store of the Copernicus Climate Change Service (Hersbach et al., 2018). We use the following weather variables: 10 m wind speed (u and v component, m/s) and direction (degrees), 2m air temperature (K), 2m dewpoint temperature (K), relative humidity (%), geopotential (m2/s2), and BLH (m). All the variables are downloaded at the original resolution of 0.25×0.25 degree and then linearly interpolated to 0.1×0.1 degree (about 10km×10km) resolution. The utilized surface NO2 data is collected from CAMS European air quality forecast and reanalyses and forecast (Marécal et al., 2015) by using the Atmosphere Data Store of the CAMS (https://ads.atmosphere.copernicus.eu/). Since the forecast data is a 3-year rolling archive from the present, we utilized the analysis data for 2019. The surface NO2 forecast data served as the predictors under the BAU scenario for 2020 to 2022. As forecast predictions do not involve an assimilation process (Barré et al., 2021), we expect no effect of the pandemic lockdown, and the impact of the armed conflict related events on air pollution was included in the surface NO2 pollution level. Both forecast and analysis data are available at the resolution of 0.1×0.1 degree. We calculated the mean values based on data from 13:00 and 14:00hours local time to represent the surface NO2 and meteorology value at the time the satellite S5P overpassed Ukraine.

3.2.4 Fire spots database and Ukraine crisis hub

In order to draw a detailed picture of the battle spots, we utilized data from Fire Information for Resource Management System (FIRMS) provided by National Aeronautics and Space Administration (NASA) and Ukraine Crisis Hub data from the Armed Conflict Location and Event Data Project (ACLED) (Raleigh et al., 2010). The NASA FIRMS portal provides active fire data at three-hour intervals based on satellite observations from products of the Moderate Resolution Imaging Spectroradiometer (MODIS) and Visible Infrared Imaging Radiometer Suite (VIIRS). For the study, data from the VIIRS product was employed to access the active fire spots due to its superior fire detection capabilities compared to the MODIS products (Csiszar et al., 2014; Schroeder et al., 2014).

Detailed data on conflict hotspot locations are extracted from the Ukraine Crisis Hub which is distributed by ACLED (Raleigh et al., 2010). Information regarding the conflict events is updated weekly and disaggregated to event type with time and location (latitude and longitude) in Ukraine and the Black Sea region available from 2018 until the present. As a result of the conflict, we expect to see and identify corresponding patterns between locations of active fire spots and the locations of conflict events.

3.2.5 Population data

As NO2 pollution levels are closely related to human socio-economic activities and frequently high in populous urban areas, we downloaded 2020 population data for Ukraine from the WorldPop Global Project (www.worldpop.org), available annually at the spatial resolution of 100m×100m as one of the features for the BAU NO2 model. The population data was collected, clipped to the Ukrainian territory, and linearly interpolated to 0.1×0.1 degree (about 10km×10km).

3.3 Business-as-usual (BAU) modelling

When considering changes induced by the pandemic lockdown and the armed conflict, especially for before-after analysis, an important factor is the meteorology variations. In this study, we use a suggested list of predictors by (Barré et al., 2021), which consists of meteorological, spatial, and temporal features, population counts from WorldPop Global Project, and surface NO2 pollution levels from CAMS European analysis data for 2019 and forecast data for 2020 to 2022 for BAU model development. The spatial and temporal features contain latitude, longitude, Julian date (number of the day from January 1), and day of the week, respectively. However, unlike the study cited (Barré et al., 2021), for machine learning model selection, instead of GBM we utilized LightGBM (Ke et al., 2017), which is a gradient boosting decision tree, to build the BAU model. During the training process, other than in studies that used the grid search with an n-fold cross-validation approach to tune the model's hyperparameters (Barré et al., 2021; Petetin et al., 2020), we employed the Fast Library for Automated Machine Learning (FLAML) (Wang et al., 2021), which is a new lightweight library for quickly determining the accurate model, to find the optimum hyperparameters for the LightGBM model in our case.

In order to assess the performance of the BAU simulation model, we randomly selected and used 80% of the data for the training set and 20% for the validation set. We used the following metrics: mean bias (MB), normalized mean bias (nMB), root mean square error (RMSE), normalized root mean square error (nRMSE) and Pearson correlation coefficient (R). As shown in the detailed results presented in Table 3.1, the model achieved high R on the validation set

Table 3.1. The performance of the BAU model on the validation set described using the following metrics: mean bias (MB), normalized mean bias (nMB), root mean square error (RMSE), normalized root mean square error (nRMSE) and Pearson correlation coefficient (R). N represents the number of points in both the training set and validation set, where each point is associated with unique latitude and longitude values. There are no duplicate points shared between the training and validation sets.

	MB	nMB	RMSE	nRMSE	R	n
Performance with S5P data version 1.x—ORG data						
Training set	3.68×10^{-5}	1.53×10^{-4}	7.80	7.40	0.87	5022
Validation set	0.03	0.10	9.53	10.98	0.80	1269
Performance with S5P data version 2.4—RPRO data						
Training set	2.67×10^{-4}	1.04×10^{-3}	6.97	5.12	0.91	5051
Validation set	0.07	0.26	8.47	7.75	0.86	1242

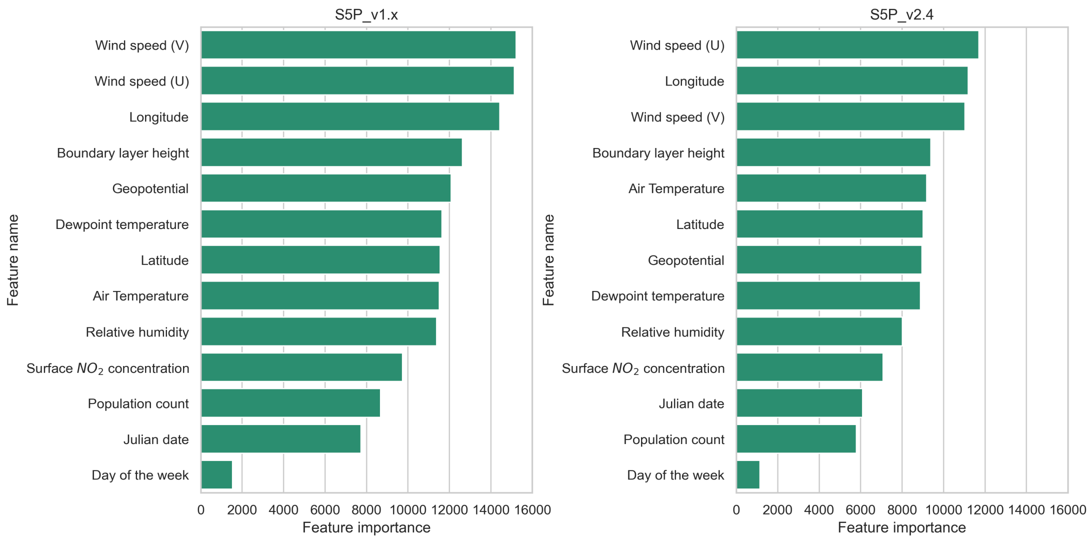

Figure 3.3. Feature importance estimated using LightGBM split method.

(0.8 for ORG data, 0.86 for RPRO data), with low MB and RMSE indicating that the column NO2 levels are well represented by the input features. Based on the feature importance measure as shown in Figure 3.3, we found that the most

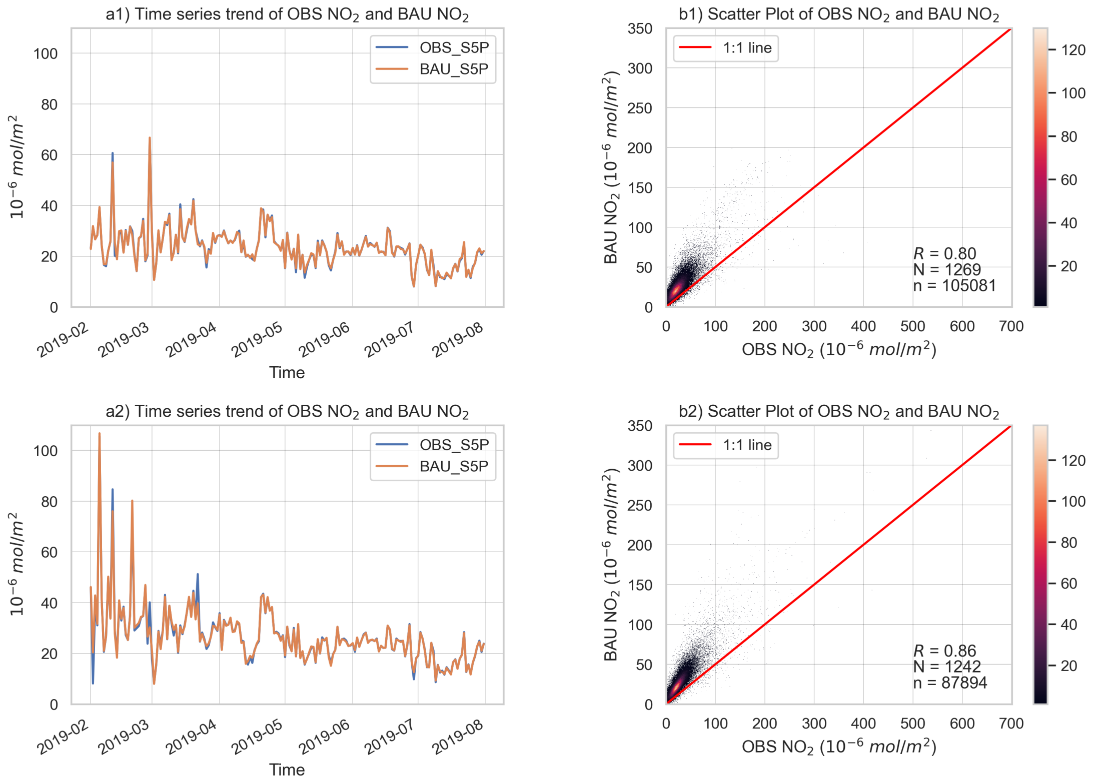

Figure 3.4. The timeseries trend lines (a1) and (a2) and scatter plots (b1) and (b2) depict the OBS NO2 and BAU NO2 on the validation set in 2019. Sub-figures (a1) and (b1) correspond tothe S5P version 1.x data, while sub-figures (a2) and (b2) represent the S5P version 2.4 data. Inthe scatter plot, we showed the 1:1 line, Pearson correlation coefficient (R), N represents thenumber of points in both the training set and validation set, where each point is associated withunique latitude and longitude values. At each point, we used the available daily data fromFebruary 1 to July 31, 2019, to make the training and validation set with total number samples isdenoted as n. There are no duplicate points and samples shared between the training andvalidation sets.

important predictors are wind speed and direction, and BLH, which is also consistent with our hypothesis about the impact of the meteorological parameters on column NO2 levels mentioned above. In Figure 3.4, we present the performance of the BAU model on the validation set using trend lines and scatter plots to

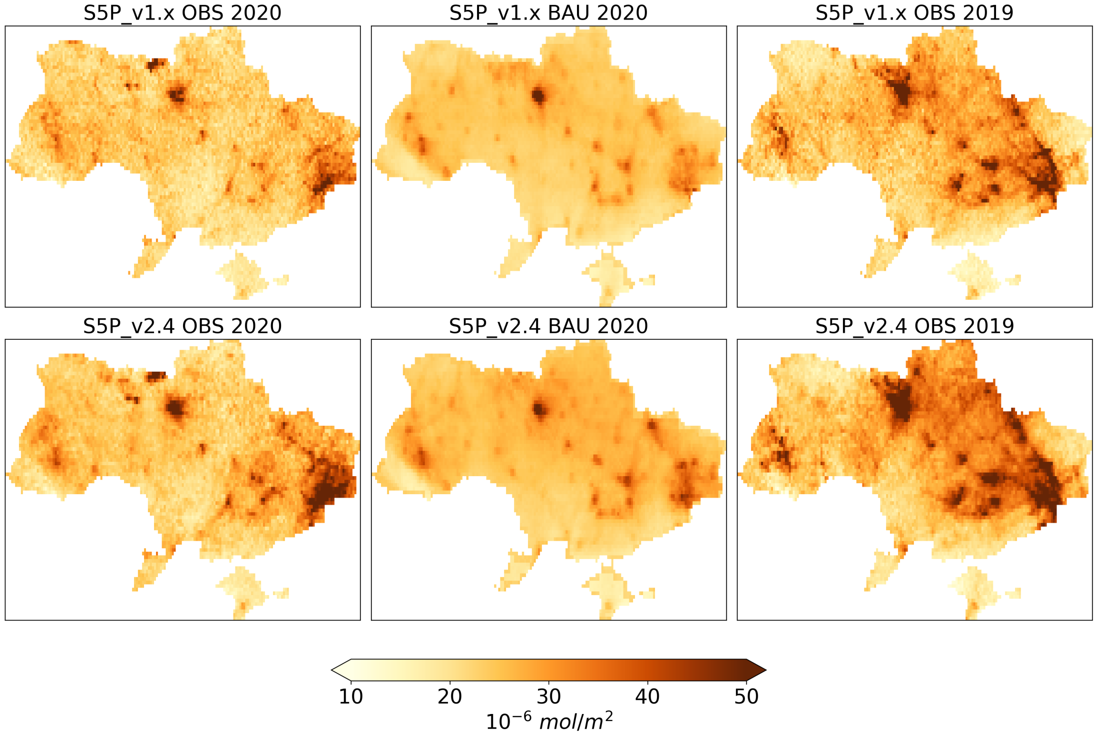

(a) The OBS, BAU data in 2020 (April 6 to May 10) with reference data in 2019

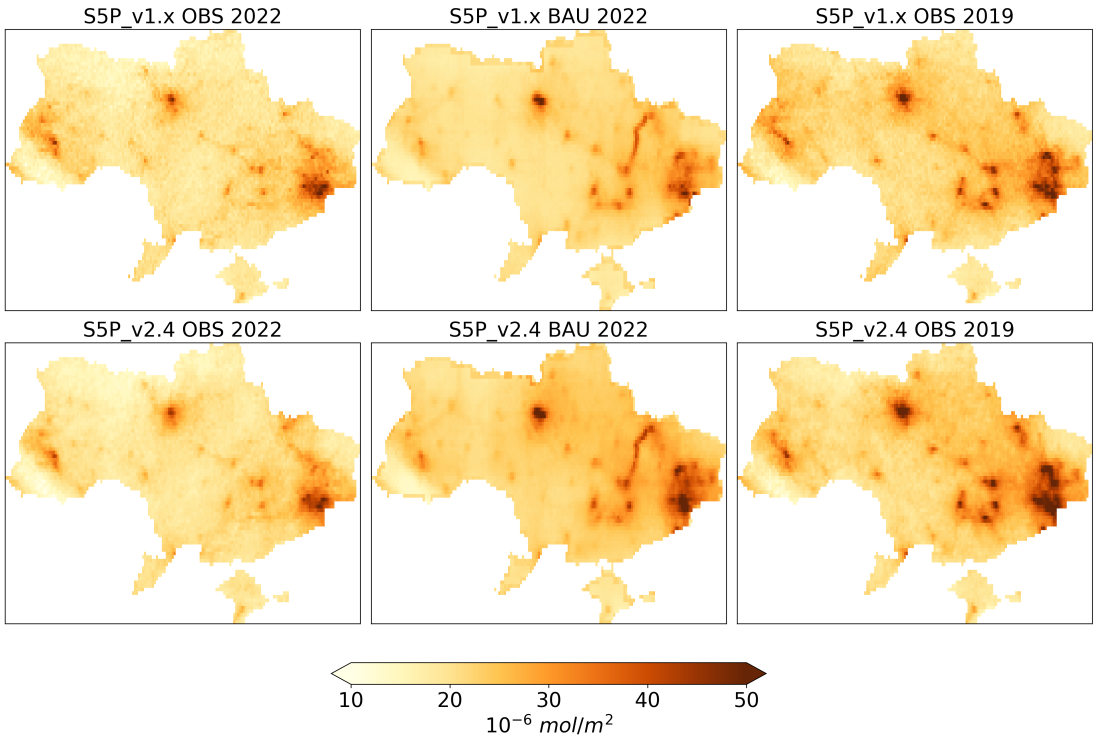

(b) The OBS, BAU data in 2022 (February 24 to July 31) with reference data in 2019

Figure 3.5. The OBS (1st column), BAU (2nd column) data from April 6 to May 10, 2020 (a)and from February 24 to July 31, 2022 (b) with the corresponding reference data in 2019 (3rdcolumn)

compare the predictions with the actual ground truth data. Furthermore, Figure 3.5 displays the OBS data, BAU model's predictions during the lockdown period in 2020, and more than five months of the conflict (February 24–July 31) in 2022. This data is accompanied by the reference NO2 levels from 2019 which were utilized to train the BAU for corresponding periods. The hyperparameters used to develop the LightGBM model are listed in Table 3.2 for S5P data version 1.x and version 2.4.

Table 3.2. The hyperparameters used to develop the LightGBM model with S5P data version 1.x and version 2.4. We used FLAML library (Wang et al., 2021) for tuning these following parameters: shrinkage rate (learning_rate), minimal number of data in one leaf (min_data_in_leaf), minimal sum hessian in one leaf (min_sum_hessian_in_leaf), number of boosting iterations (num_iterations), max number of leaves in one tree (num_leaves).

Parameter	S5P v1.x	S5P v2.4
learning_rate	0.30775042929674906	0.3858774543125185
min_data_in_leaf	11	5
min_sum_hessian_in_leaf	0.001	0.001
num_iterations	907	3451
num_leaves	8604	4342

The main shortcoming of this method is the lack of qualified reference data to develop the weather normalization model under BAU conditions, as the S5P TROPOMI data has been only available since mid-2018. Only one year of training data in 2019 is considered relatively small, thus resulting in large errors in BAU simulations in winter months as during this time, limited qualified S5P observations are available and NO2 pollution levels are quite unpredictable due to the inconsistency in heating activities and NO2 intake from Poland.

3.4 COVID-19 induced NO2 changes

The purpose of this section is to examine the effect of the lockdown on changes in NO2 column levels in populous urban areas, namely the nine cities Kyiv, Kharkiv, Odessa, Dnipro, Donetsk, Zaporizhzhia, Lviv, Kryvyi Rih, and Mykolaiv (listed in declining order of population). To begin, we analyse the meteorological patterns during the pre-lockdown and lockdown periods and discuss how these might influence the NO2 levels, apart from the impacts of the lockdown measures. Next, we utilize two methods to estimate changes in NO2 levels. The first method, known as the year-to-year approach suggested by (Barré et al., 2021), involves calculating the median value of the actual S5P observation data in 2020 and subtracting the observation data from 2019. The second method, OBS-BAU, utilizes the median value of the actual observation data (OBS) in 2020 and subtracts the simulated NO2 levels that represent the BAU scenario, which are predicted by the S5P tropospheric NO2 column levels without any lockdown measures. The BAU simulations are based on the representation of meteorological, spatial, and temporal parameters.

3.4.1 Lockdown and pre-lockdown meteorological patterns

Figure 3.6a and 3.6b display the probability density functions of the BLH, and Figure 3.6c and 3.6d display wind speed and direction during the pre-lockdown and lockdown periods of 2019 and 2020 based on data from the nine selected cities. In 2020, the BLH exhibited a similar distribution to that of 2019 during the pre-lockdown period, but with lower values. This decrease in BLH would have resulted in an increase in NO2 levels in 2020 compared to 2019, as the reduced BLH restricts the dispersion of NO2 emissions, leading to an increase in NO2 concentration levels (see Figure 3.6a).

Conversely, during the lockdown period (see Figure 3.6b), we observed higher values of BLH in 2020 compared to 2019. This increase in BLH could have contributed to the dispersion of NO2 concentration, resulting in a reduction of NO2 levels during the lockdown in 2020. This phenomenon, in addition to the effects of the lockdown restrictions, may have also contributed to minimizing the NO2 levels over major cities in Ukraine. Therefore, it is essential to consider the impacts of meteorological variables on NO2 level variability analysis.

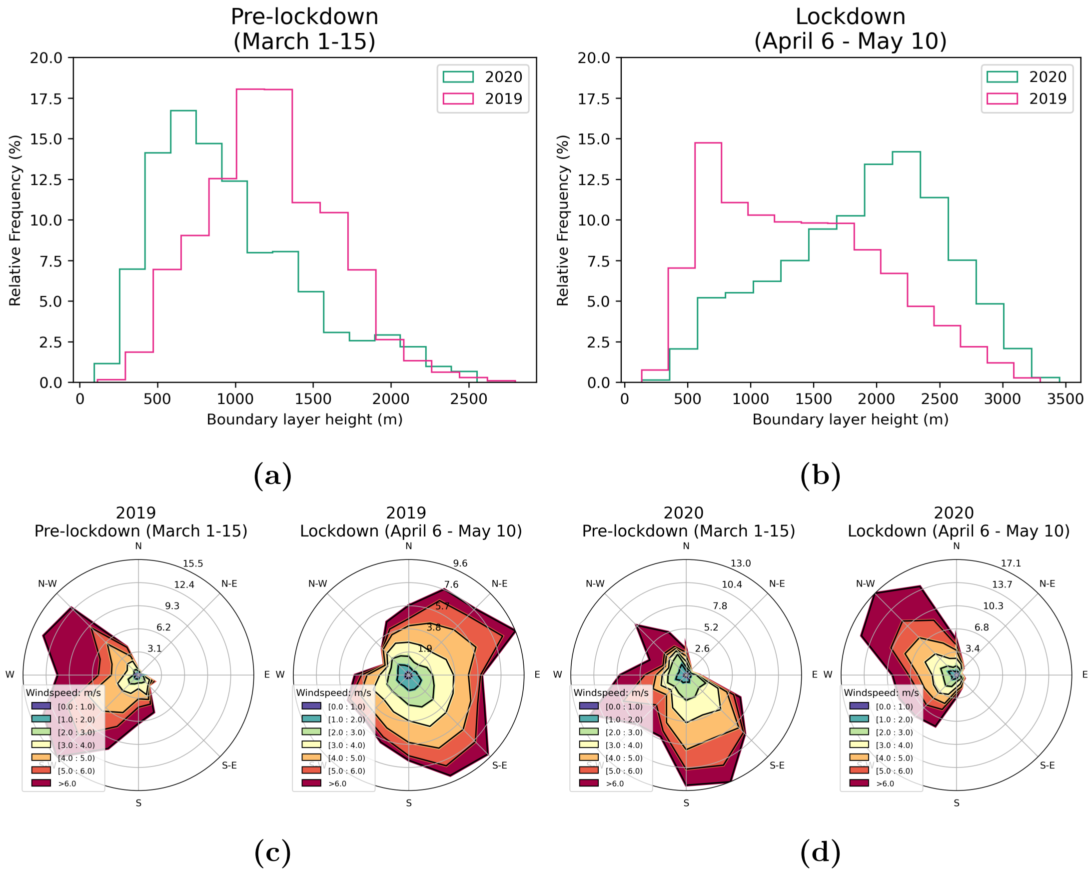

Figure 3.6. Probability density functions of BLH during (a) the pre-lockdown (March 1–15) and (b) the lockdown period (April 6–May 10) between 2019 and 2020 based on data from the nine most populous cities of Ukraine. Wind rose plots for wind speed and direction for pre-lockdown (March 1–15) and lockdown (April 6–May 10) periods in (c) 2019 and (d) 2020 based on data from the nine most populous cities of Ukraine

3.4.2 NO2 changes in populous Ukrainian cities

In Figures (3.7a, 3.7b), and Table 3.3, we present the result of the year-to-year approach. We assumed that there would be a minimal change in NO2 pollution levels during the pre-lockdown period, but a significant reduction during the lockdown when comparing the same time frame in 2019 and 2020 due to the implemented lockdown measures and social distancing practices. In Figure 3.7, two different methods, namely the OBS-BAU and year-to-year approaches, were used for the analysis. The circle size in the figures corresponds to the population of each city. For each sub-figure (a) and (b), the first row (a1, a2, b1, b2) contains two plots showing the results based on the ORG data (S5P v1.x), while the second row (a3, a4, b3, b4) includes two plots presenting the results based on the RPRO data (S5P v2.4). The left column plots (a1, a3, b1, b3) of Figures (3.7a, 3.7b) display the year-to-year estimates, while the right column plots (a2, a4, b2, b4) display the OBS-BAU estimates. Figure 3.7a illustrates that the prevailing trend in the nine selected cities during the pre-lockdown period showed an increase, with an average of 5.2% (ORG data) and 13.9% (RPRO data) in NO2 levels, while during the lockdown period (Figure 3.7b), a general reduction was observed in most cities with an average of 15.6% (ORG data) and 11.1% (RPRO data). This confirms that the lockdown measures reduced the NO2 column concentrations in major urban areas of Ukraine, as we anticipated. It is worth noting that the year-to-year approach using the original satellite observations has been widely used in many studies and online resources. However, as mentioned in (Barré et al., 2021; Grange et al., 2021), it is heavily influenced by meteorological variables such as wind speed and direction, and BLH (Wallace and Kanaroglou, 2009).

In order to quantify the true improvement in air quality with respect to column NO2 levels due to the lockdown restrictions, we calculated the difference between the actual observation data and the simulated data under BAU conditions with the meteorological effects decoupled. Like the year-to-year approach, we anticipate a slight variation between the OBS NO2 levels and the BAU NO2 levels during the pre-lockdown period. Furthermore, we expect to observe an overall reduction in the OBS data compared to the BAU data, or at least, a lesser increase during the lockdown when compared to the pre-lockdown levels, due to the impact of the lockdown measures. Figure 3.7((a2, a4) and (b2, b4)) shows the OBS-BAU estimates for pre-lockdown and lockdown in 2020. During the pre-lockdown (Figure 3.7(a2, a4)), we observed an average increase of 3.7% (ORG data) and 12.5% (RPRO data), which is smaller than the year-to-year estimate. However, during the lockdown period (Figure 3.7(b2, b4)) a smaller increase trend was observed, with an average of 0.5% (ORG data) and 10.2% (RPRO data). This indicates that while the OBS NO2 levels in 2020 were higher than those predicted under the

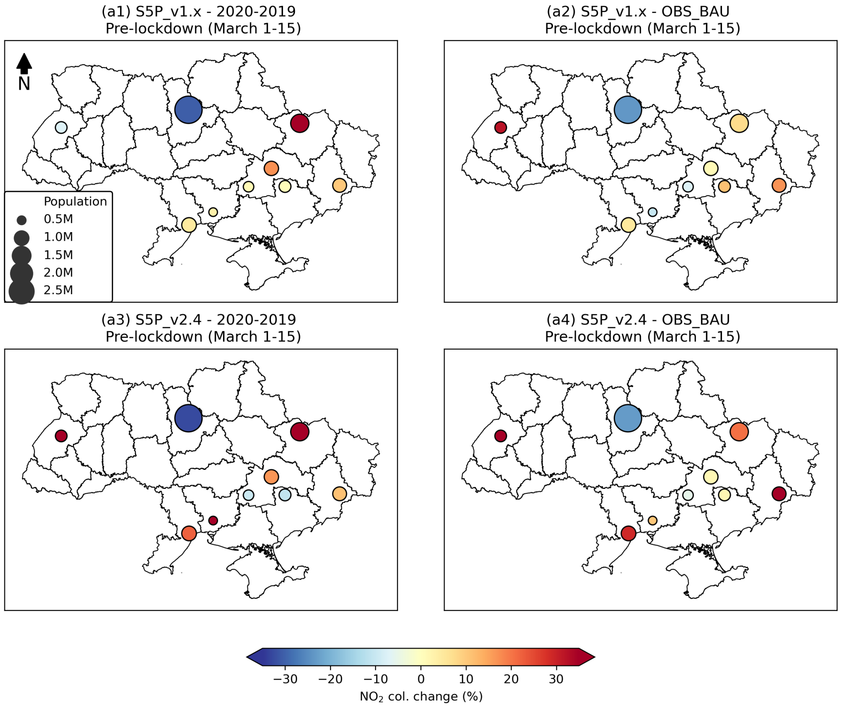

(a) Pre-lockdown period

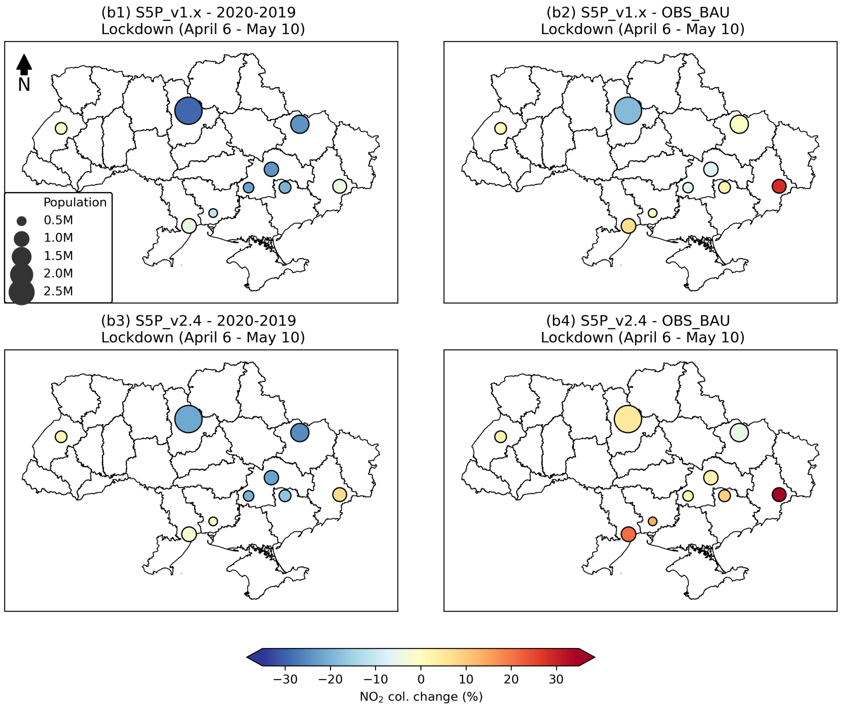

(b) Lockdown period

Figure 3.7. Estimates of S5P NO2 column changes for the nine most populous cities in Ukraine during the (a) pre-lockdown and (b) lockdown periods.

Table 3.3. The OBS-BAU and year-to-year (2020–2019) estimates (in percentage) during pre-lockdown and lockdown periods in the nine most populous cities in Ukraine. The values are represented as mean, while standard deviation is not presented here due to lack of space.

City	Pre-lockdown (March 1 −15)				Lockdown (April 6 −May 10)			
	OBS-BAU		2020−2019		OBS-BAU		2020−2019	
	ORG	RPRO	ORG	RPRO	ORG	RPRO	ORG	RPRO
Kyiv	−23.7	−23.1	−30.6	−32.8	−18.8	4.9	−29.4	−21.4
Kharkiv	7.6	20.8	47.9	49.1	−0.9	−4.9	−24.1	−24.9
Odessa	5.1	29.0	4.8	22.4	6.9	21.0	−4.4	−1.9
Dnipro	1.3	1.5	17.0	16.7	−6.6	2.8	−23.9	−22.3
Donetsk	16.8	41.9	10.3	11.2	28.2	42.0	−4.0	7.2
Zaporizhzhia	11.5	1.9	0.6	−11.1	2.5	9.1	−20.1	−17.2
Lviv	32.2	35.7	−7.3	37.7	0.0	3.0	−1.2	1.4
Kryvyi Rih	−7.3	−5.3	1.2	−9.8	−6.4	0.1	−21.9	−20.5
Mykolaiv	−10.2	10.1	3.3	41.5	−0.6	13.8	−11.1	−0.4
Mean	3.7	12.5	5.2	13.9	0.5	10.2	−15.6	−11.1

BAU scenario during the lockdown period, the measures implemented during the lockdown effectively curbed the increase in NO2 column concentrations in major urban areas of Ukraine when compared to the pre-lockdown levels, aligning with our initial expectations. By using the OBS-BAU estimate based on the ORG data, the most significant reduction was observed in Kyiv (18.8%), with Dnipro and Kryvyi Rih experiencing smaller reductions of 6.6% and 6.4%, respectively. However, when using RPRO data, a reduction was only seen in Kharkiv (4.9%).

In comparison with the year-to-year approach with respect to the pre-lockdown (see Table 3.3), the OBS-BAU estimates (3.7% for ORG data, 12.5% for RPRO data) show a smaller change than in year-to-year estimates (5.2% for ORG data, 13.9% for RPRO data). We consider the OBS-BAU estimate to be more reasonable as mentioned above, and the lower values in BLH in 2020 could result in higher year-to-year estimates during the pre-lockdown period between 2020 and 2019. Therefore, we anticipate a lower estimate, which is a smaller increase, after the weather effects are decoupled. Similar findings are seen during the lockdown for OBS-BAU and year-to-year estimates. The contribution from the lower BLH in 2019 could overestimate the reduction of NO2 concentrations by 15.6% (ORG data) and 11.1% (RPRO data) in the year-to-year lockdown estimates. By normalizing the weather effects, a lower reduction in the increase is anticipated and estimated from the OBS-BAU approach (0.5% for ORG data, 10.2% for RPRO data). Additionally, the year-to-year approaches mostly present a larger standard deviation than the OBS-BAU approach, which could be attributed to local biases caused by meteorological variabilities (Barré et al., 2021). Using weather-normalization techniques, we observed that much of the reduction in NO2 levels between 2020 and 2019 can be attributed to weather variability. This suggests that stricter measures may need to be considered in the future to achieve significant NO2 reductions in densely populated areas of Ukraine.

3.5 NO2 changes induced by the armed conflict

In the previous section, we discussed the influence of meteorological factors on the concentration of NO2 and how using OBS-BAU estimates can mitigate overestimation or underestimation in the year-to-year approach. In this section, we shift our focus solely to the OBS-BAU estimates to explore the impacts of the armed conflict on NO2 column concentration. The year-to-year estimates are displayed together for the purpose of comparison.

During the lockdown, one might reasonably assume that pollution levels were likely to decrease as the result of an anticipated reduction in socio-economic activities in major urban areas. However, trends in NO2 levels during the conflict are likely to be unpredictable in the chaos of armed conflict actions and regionally attributed to various type of emissions at multiple locations, especially at the beginning of the conflict. On one hand, the NO2 levels should be expected to decline as anthropogenic emissions would be expected to decline due to minimized activities in transportation, industry and other socio-economic activities. On the other hand, surges in conflict activities – such as attacks with missiles, artillery shelling, bomb and mine explosions, etc., as well as the constant usage of military vehicles and the transportation of civilian populations from conflict zones in such a short time – could result in a rise in air pollution levels. Therefore, we extend our study beyond the most populous cities and include other territories in Ukraine affected by the conflict. To accomplish this, we begin by locating the conflict hotspots where military actions and battles took place, and then analyse the changes in NO2 concentrations in the hotspots, which are highly contested zones. We estimated the changes in pollution levels from individual conflict points, and the results are presented in Section 5.1. In Section 5.2, we analyse the impacts of the conflict on NO2 levels in other affected regions, such as major cities with populations exceeding 0.5 million, and the areas surrounding CPPs.

3.5.1 S5P NO2 level changes in conflict hotspots

Satellite-captured fire spots and statistics in conflict hotspots

To understand the distribution of conflict hotspots, we utilized both the satellite-capture fire data from the NASA FIRMS portal, and in particular, the locations of battles provided by ACLED (Raleigh et al., 2010). First, we inspect the fire data from the VIIRS fire product for two consecutive years (2021 and 2022), searching for patterns representing the appearance of conflict hotspots. Then, we visually compare the pattern of fire spots captured by satellite with the reported battle locations.

Figure 3.8 displays the satellite-captured fire spots for 2021 (1st column), 2022 (2nd column) and locations of conflict hotspots (3rd column). We only show the similar patterns captured from the monthly NASA FIRMS product and the reported conflict hotspot locations from Ukraine Crisis Hub, to avoid the overwhelming plots of 12 months. We observe that from February 24 until the end of March, the distribution of the detected fire spots forms no certain pattern and is scattered over the Ukrainian territory. From April to July 2022 the fire pattern starts to form and gradually be identifiable as similar to the conflict spots in the eastern part of the Ukrainian territory, while no special pattern is found in the 2021 figures for the corresponding periods. It is notable that the eastern region comprising of five oblasts (typically translated as regions or provinces, namely Dnipropetrovsk, Donetsk, Kharkiv, Luhansk, and Zaporizhzhia) has been at the frontline of the armed conflict and subject to intense conflict hotspots since the conflict began. Given our understanding that the ongoing armed conflict is the

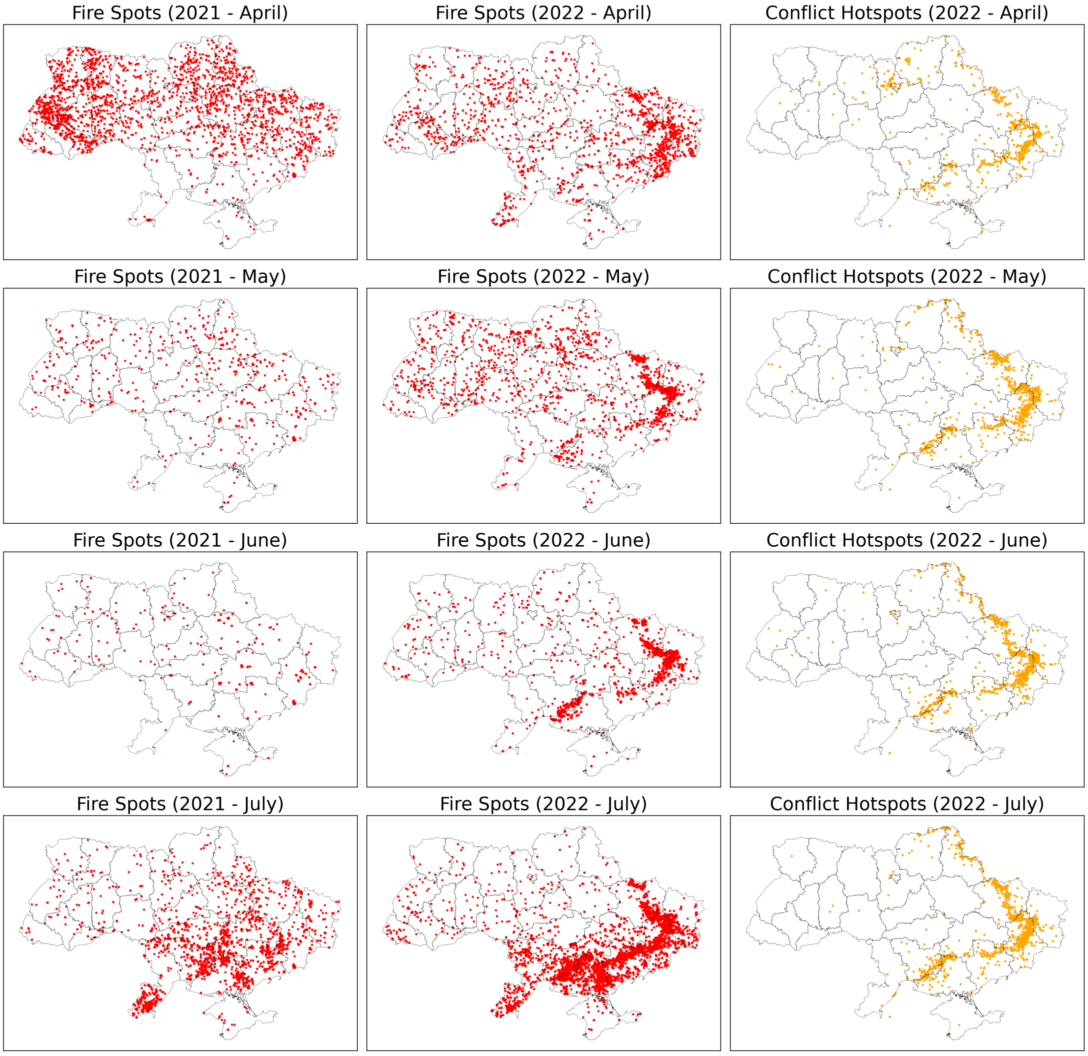

Figure 3.8. Satellite-captured fire spots for 2021 (1st column), 2022 (2nd column) and conflict hotspots (3rd column) in April, May, June and July. The patterns of conflict hotspots are clearly recognizable in the satellite-capture fire product from NASA FIRMS

source of explosions and smoke, it is reasonable to assume that the conflict has resulted in a significant increase in air pollution (Pereira et al., 2022), particularly in the areas directly affected by the conflict events that are detectable via VIIRS satellite products, so we would expect that S5P observations have the capability to show the resulting impacts on both overall air quality and concentrations of

NO2 in the affected areas.

Changes of S5P NO2 column levels

Until March 2023, as reported by (Nichita and Ana, 2023), nearly 40,000 events related to the conflict were recorded across the Ukrainian territory by the ACLED project (Raleigh et al., 2010). The five oblasts Dnipropetrovsk, Donetsk, Kharkiv, Luhansk and Zaporizhzhia have been on the frontline of the Russia-Ukraine armed conflict since February 24, 2022. In these areas, shelling, artillery, and missile attacks accounted for 71% of conflict events recorded between February 24 and July 31, 2022 (Nichita and Ana, 2023). In order to evaluate the impacts of conflict events at the smallest level, we quantify changes in NO2 column levels directly at the reported event location using OBS-BAU and year-to-year estimates for the corresponding pixel from S5P data, which is equivalent a 10 km2-area containing the event location (Figure 3.9).

The OBS-BAU estimates based on ORG data indicate an average increase of 0.3%, while the year-to-year estimates show a more substantial increase of 13.2%. However, when using RPRO data, we observed an 11% reduction in the OBS-BAU estimate and a 1.35% increase in the year-to-year estimate. Although there is a high level of uncertainty in estimating changes at the event location-pixel level, and the inconsistent timing between the reported conflict related events and S5P overpass may lead to an underestimation of changes in air pollution levels, the information gathered can still be useful in identifying changes in the NO2 columns associated with conflict related event locations in the five oblasts.

3.5.2 Changes of S5P NO2 levels in other affected areas

Most populous cities of Ukraine

In the nine most populous cities in Ukraine, both the lockdown and the conflict have led to a reduction in daily anthropogenic activities. Although this reduction was expected to lower the NO2 levels, as discussed in Section 4, the lockdown measures did not result in a significant reduction in NO2 column levels in 2020. To quantify the changes caused by the conflict and compare them with the effects of the lockdown measures, we analysed the OBS-BAU estimate for the most

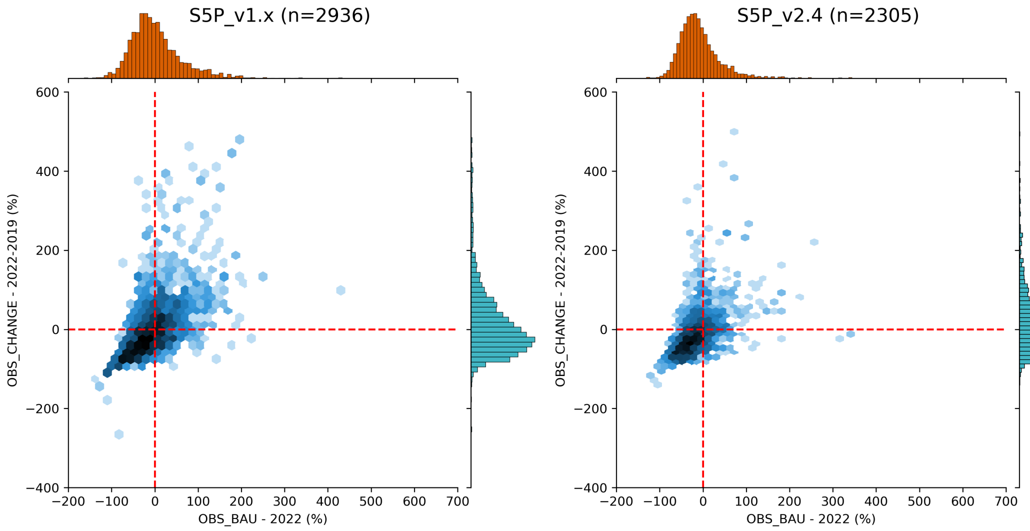

(a) **(b)**

Figure 3.9. OBS-BAU and year-to-year estimates for the individual conflict events including air/drone strikes, armed clashes, remote explosive/landmine occurrences, shelling/artillery/missile attacks, and other forms of attacks that occurred between February 24 and July 31, 2022, for five frontline oblasts, Dnipropetrovsk, Donetsk, Kharkiv, Luhansk and Zaporizhzhia. The number of data points is denoted by (n).

populous cities in Ukraine during the strict lockdown period from April 6 to May 10 in 2020 and 2022 (Table 3.4). To avoid overwhelming plots, Figure 3.10 displays the NO2 column trend lines for OBS data and BAU predictions from February to July in 2020 and 2022 for five cities (Kyiv, Kharkiv, Dnipro, Zaporizhzhia, and Kryvyi Rih) only.

Table 3.4 presents the OBS-BAU estimates corresponding to the strict lockdown period (April 6 to May 10) in 2020 and 2022 for the nine most populous cities in Ukraine. Our findings indicate that the conflict has caused more significant reductions in NO2 levels, compared to the lockdown measures. While minor reductions to increases were observed during the 2020 lockdown, a consistent and continuous reduction has been noticed in most cities, during the same lockdown period (April 6 to May 10) in 2022. The average reduction across all the cities of interest, as shown in Table 3.4, is about 12.1% (based on ORG data) and 18.1%

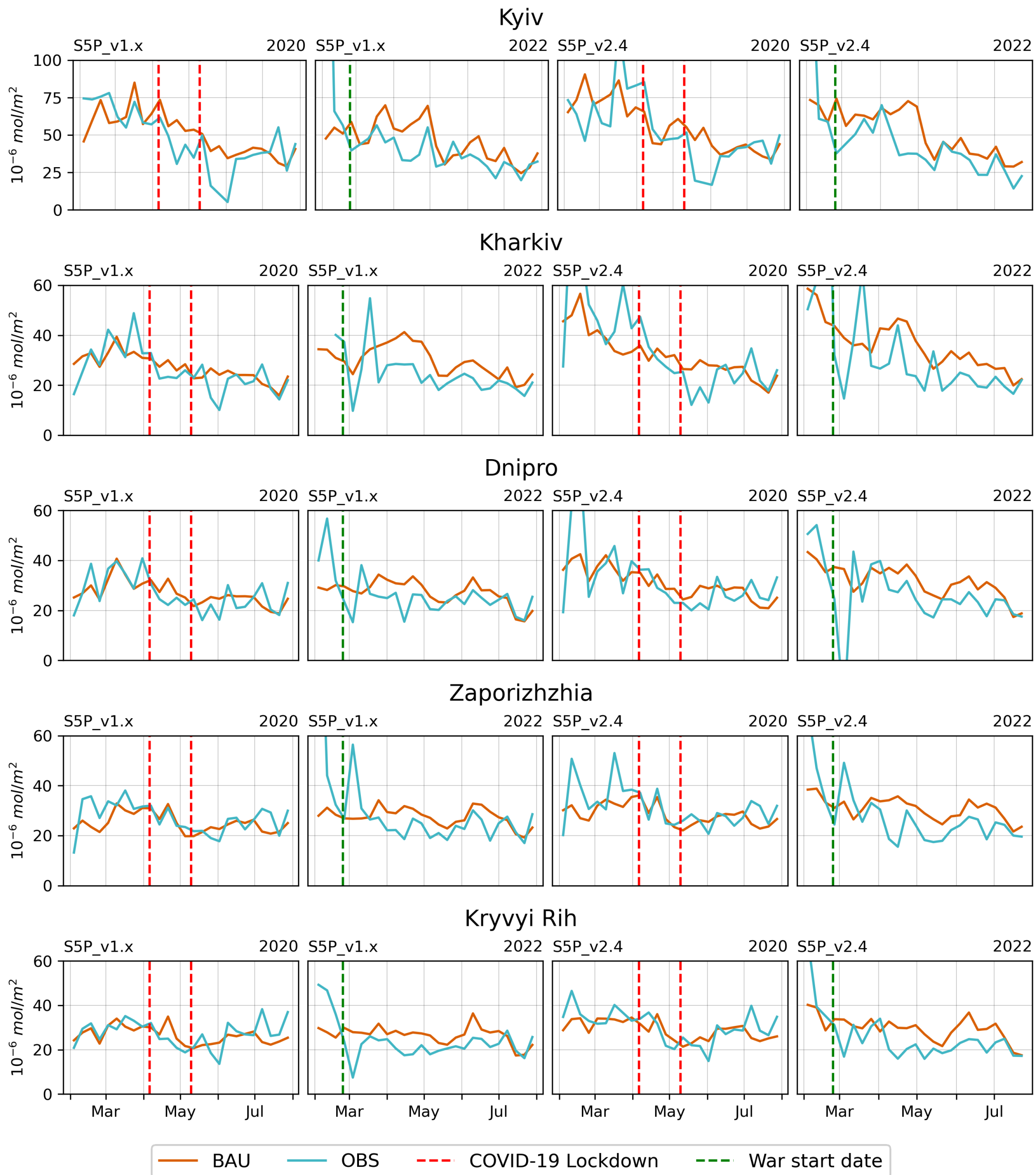

Figure 3.10. The trend lines of OBS and BAU S5P NO2 column levels from February to July in 2020 and 2022 for five cities in Ukraine. Each row displays plots for a different city. The first and second column plots represent the ORG data (S5P version 1.x), while the third and last column plots show the RPRO data (S5P version 2.4). The first and third column plots pertain to 2020, while the second and last column plots pertain to 2022.

Table 3.4. The OBS-BAU estimate (in percentage) of ORG data and RPRO data for the strict lockdown period (April 6 to May 10) in 2020 and in 2022 for the nine most populous cities in Ukraine. The values are represented as mean (with standard deviation in parentheses). The mean and standard deviation in the last row were calculated across the nine cities.

City	2020 (April 6 –May 10)		2022 (April 6 –May 10)	
	ORG	RPRO	ORG	RPRO
Kyiv	–18.8 (6.5)	4.9 (17.4)	–29.3 (9.5)	–34.6 (7.6)
Kharkiv	–0.9 (10.3)	–4.9 (15.9)	–24.9 (17.9)	–29.7 (20.8)
Odessa	6.9 (12.4)	21.0 (16.4)	–7.6 (14.3)	–14.5 (9.7)
Dnipro	–6.6 (9.2)	2.8 (10.9)	–17.4 (10.0)	–19.5 (8.6)
Donetsk	28.2 (35.2)	42.0 (29.8)	3.5 (19.9)	3.2 (18.7)
Zaporizhzhia	2.5 (9.1)	9.1 (12.7)	–12.6 (13.7)	–18.4 (11.6)
Lviv	0.0 (10.9)	3.0 (8.5)	14.9 (17.9)	–3.3 (9.9)
Kryvyi Rih	–6.4 (8.7)	0.1 (9.9)	–20.8 (9.8)	–27.7 (8.1)
Mykolaiv	–0.6 (9.8)	13.8 (17.6)	–14.6 (10.1)	–18.0 (6.8)
Mean	0.5 (11.9)	10.2 (13.3)	–12.1 (13.2)	–18.1 (11.5)

(based on RPRO data). The largest reduction was observed in Kyiv, while the increase occurred in Lviv (14.9% based on ORG data) and in Donetsk (3.5% based on ORG data, 3.2% based on RPRO data).

In more than the first five months after the conflict began until the end of July 2022, an overall reduction is observed across the nine cities (see Table 3.5) with an average of 3.1% (ORG data) and 7% (RPRO data). The largest reductions in NO2 levels were observed in Kyiv, with an average of 14.9% (ORG data) and 27.6% (RPRO data). Conversely, Donetsk and Lviv experienced increases in NO2 levels, with both ORG and RPRO data, while in Mykolaiv only RPRO data showed the increases. The rise in Donetsk can be attributed to it being where major armed conflicts occurred during this period.

Table 3.5. Average OBS-BAU and year-to-year estimate (in percentage) of ORG data and RPRO data from February 24 to July 31, 2022, for the nine most populous cities in Ukraine. The values are represented as mean (with standard deviation in parentheses). The mean and standard deviation in the last row were calculated across the nine cities.

City	ORG		RPRO	
	OBS-BAU	year-to-year	OBS-BAU	year-to-year
Kyiv	−14.9 (17.3)	−30.5 (14.7)	−27.6 (12.1)	−37.3 (11.3)
Kharkiv	−3.2 (28.5)	20.7 (39.8)	−3.0 (33.3)	2.4 (23.6)
Odessa	−6.8 (15.4)	−13.6 (16.4)	−5.4 (13.0)	4.5 (61.0)
Dnipro	−12.4 (16.6)	−15.0 (21.3)	−17.6 (13.8)	−17.0 (20.5)
Donetsk	19.4 (26.6)	4.2 (21.5)	17.0 (22.8)	−9.4 (15.8)
Zaporizhzhia	−10.5 (16.4)	−15.7 (27.3)	−13.7 (14.4)	−19.1 (18.6)
Lviv	20.8 (21.9)	−9.0 (24.1)	2.2 (16.8)	−9.8 (17.3)
Kryvyi Rih	−15.5 (15.7)	−22.4 (21.7)	−17.4 (15.0)	−26.2 (42.7)
Mykolaiv	−4.8 (13.1)	−7.8 (23.5)	2.1 (14.8)	12.9 (21.9)
Mean	−3.1 (13)	−9.9 (14.1)	−7 (12.7)	−11 (15)

Coal power plants

Besides anthropogenic activities in major cities, the contribution of CPPs to NO2 concentration levels is considered to be significant in Ukraine (Lauri and Rosa, 2021). The Zaporizhzhia CPP is one of the largest emitters among CPPs in Ukraine, emitting 21,830 tonnes of NOx in 2019. Many power plants have been targeted in the conflict, and their damage or destruction has resulted in power blackouts affecting millions of people.

According to Draft Ukraine Recovery Plan, Materials of the "Energy Security" Working Group covering the period to the end of June 2022, significant damage has been reported at the Zaporizhzhia, Luhansk, and Sievierodonetsk power stations, as well as other CPPs. This damage could be expected to affect NO2 levels in the areas surrounding the damaged power plants. To investigate such changes, we also compare trends in the NO2 column levels between OBS data and BAU simulations for 2020 and 2022, utilizing both ORG and RPRO data as presented

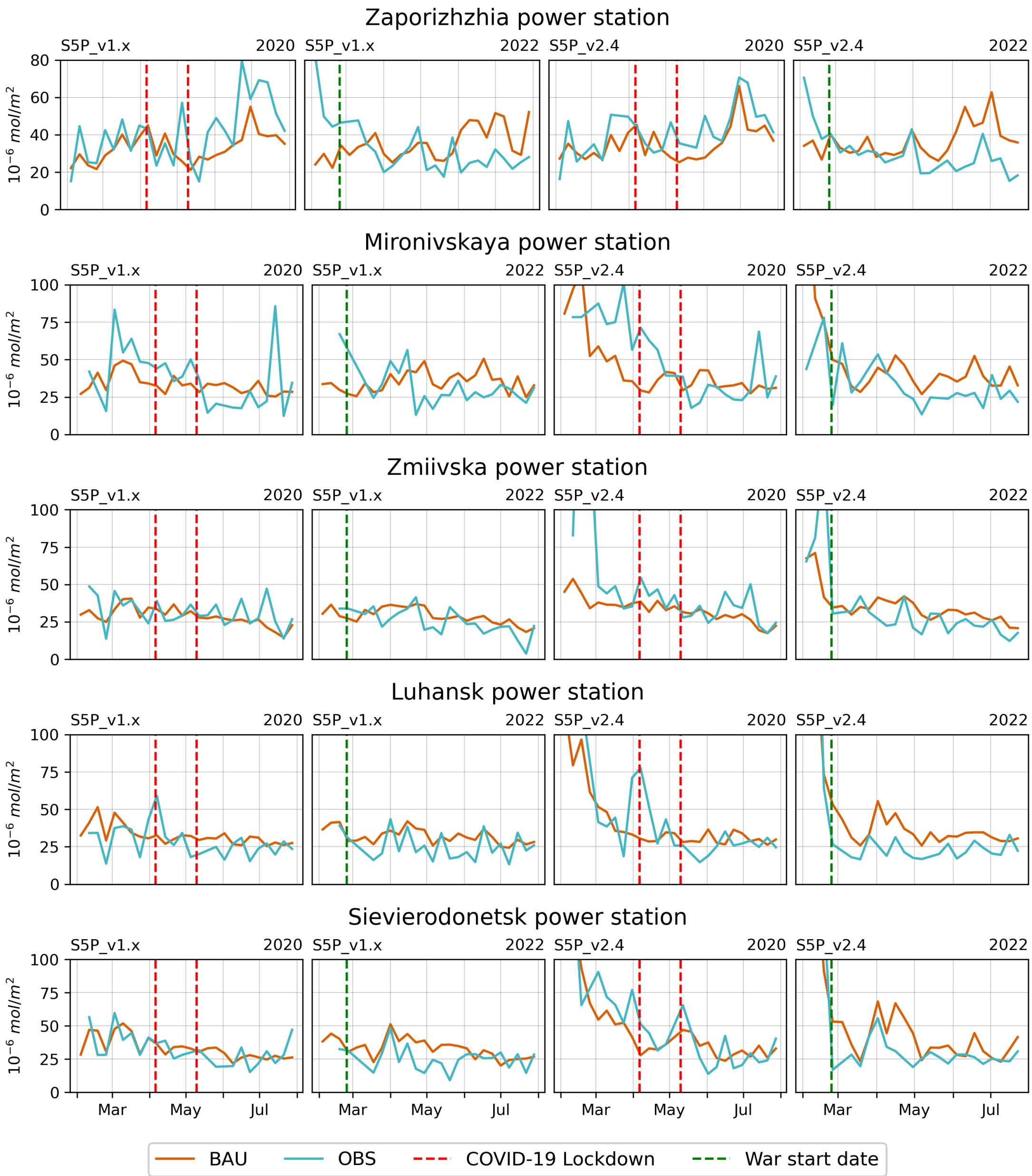

Figure 3.11. The trend lines for the OBS and BAU S5P NO2 column levels from February to July in 2020 and 2022 are presented for selected CPPs. Each row displays plots for a different CPP. The first and second column plots represent ORG data (S5P version 1.x), while the third and last column plots show RPRO data (S5P version 2.4). The first and third column plots pertain to 2020, while the second and last column plots pertain to 2022.

in Figure 3.11. Examining an area of 10km2 around each CPP, we find that, similar to previous discussions on lockdown effects, little changes are observed around most CPPs during the pandemic lockdown in 2020. However, a clear reduction is evident between the time when the conflict began and July 2022 at the Zaporizhzhia, Mironivskaya, Zmiivska, Luhansk, and Sievierodonetsk power stations. At areas surrounding other power stations, no noticeable reduction is observed.

3.6 Conclusion

In this study, we performed a comprehensive assessment of variations in the S5P column NO2 levels in Ukraine during the COVID-19 pandemic lockdown in 2020 and the armed conflict with Russia in 2022. For this purpose, we utilized two S5P products, namely, original and reprocessing data. We first developed a weather normalization model under business-as-usual conditions, using meteorological parameters from ERA5 reanalysis, ensembled surface forecasts, and analysis NO2 data from 11 CAMS models, along with other spatial and temporal features. Next, we applied the BAU prediction to estimate the change in NO2 levels during the lockdown period in 2020 for the nine most populous cities in Ukraine (Kyiv, Kharkiv, Odessa, Dnipro, Donetsk, Zaporizhzhia, Lviv, Kryvyi Rih, and Mykolaiv). We extended the analysis using BAU predictions to estimate the impact of the armed conflict from February 24 to July 31, 2022, in conflict hotspot locations, the nine most populous cities, and areas surrounding selected CPPs (Zaporizhzhia, Mironivskaya, Zmiivska, Luhansk, and Sievierodonetsk) in Ukraine.

The main outcomes of the study can be summarized as follows:

- In 2020, meteorological parameters also heavily influenced the NO2 tropospheric column levels, contributing to decreases in levels during the lockdown period.

- After normalizing the meteorological parameters, we found that the lockdown did not lead to lower NO2 levels than the BAU prediction in 2020, although it did manage to mitigate the increase in NO2 compared to the pre-lockdown period. Our study indicates that stricter measures may need to be considered in the future to achieve a significant reduction in NO2 levels in densely populated areas of Ukraine.

- We observed that satellite-capture fire data from the VIIRS product can capture the spatial patterns of the conflict related events on the ground. From this product, conflict location patterns are clearly represented during the April–July 2022 period.

- Upon examining changes in NO2 levels at conflict hotspots at the location-pixel level, we observed changes ranging from an 11% reduction to a slight increase of 0.3% when comparing the OBS to BAU predictions using RPRO and ORG data, respectively.

- During the strict lockdown period from April 6 to May 10, 2022, the reduction in NO2 levels in the nine most populous cities was more significant compared to 2020. Across most cities, an average reduction of 12.1% (ORG data) and 18.1% (RPRO data) was observed. However, it is worth noting that Lviv and Donetsk showed an increase in NO2 levels during this period.

- From February 24 to July 31, 2022, the nine most populous cities in Ukraine experienced an overall reduction of 3.1% (ORG data) and 7% (RPRO data) in NO2 levels. The most significant reduction was observed in Kyiv, with an average decrease of 14.9% (ORG data) and 27.6% (RPRO data). However, in contrast, NO2 levels increased in Lviv, Donetsk and Mykolaiv during this period.

- The conflict has resulted in damage to several CPPs, which are considered as major sources of NO2 emissions in the country. Our analysis indicates a clear reduction in NO2 levels in the areas closely surrounding Zaporizhzhia, Mironivskaya, Zmiivska, Luhansk, Sievierodonetsk CPPs.

- By utilizing the OBS-BAU estimate for both ORG data and RPRO data to analyse NO2 variations during the 2022 conflict, we found that discrepancies resulting from changes in the processor during the S5P lifetime in ORG data might lead to a slight underestimation of NO2 reductions. Specifically, we observed a smaller decrease using ORG data (3.1%) than with RPRO data (7%) in the most populous cities of Ukraine.

The consideration of meteorological effects is crucial in regulating pollution levels. Neglecting these effects could introduce errors in quantifying actual air quality changes attributed to an intervention event. For future studies assessing the impacts of conflict in Ukraine on air quality, it will be essential to account for meteorological variability to achieve genuine and quantitative estimates.

NO2 is a significant precursor to tropospheric O3 and also affects the lifetime of methane (CH4) (Akimoto and Tanimoto, 2022). Additionally, it has the potential to serve as an indicator for monitoring CO2 emissions (Miyazaki and Bowman, 2023). In future studies, it would be valuable to explore how changes in NO2 levels during conflict could impact O3 and CH4 concentrations in Ukraine as both are important short-lived climate pollutants that contribute to positive radiative forcing, thereby exacerbating global warming.

4 Japan's case study

4.1 Introduction

Nitrogen dioxide (NO2) is an important air pollutant that raises significant concerns due to its negative effects on human health (Hamra et al., 2015). Additionally, it serves as a crucial precursor to tropospheric ozone (O3), along with volatile organic compounds (VOCs) (Akimoto and Tanimoto, 2022). Nitrogen oxides (NOx = NO + NO2), carbon monoxide (CO) and non-methane volatile organic compounds (NMVOCs) have an influence on the methane (CH4) lifetime by affecting the atmospheric mixing ratio of hydroxyl radicals (OH) (Akimoto and Tanimoto, 2022), which act as a primary sink for CH4 (Turner et al., 2019). Both O3 and CH4 are short-lived climate pollutants (SLCPs) that contribute to positive radiative forcing, thereby intensifying global warming (Akimoto and Tanimoto, 2022). Moreover, owing to its short lifetime in the atmosphere and significant signal compared to carbon dioxide (CO2), NO2 possesses the potential to serve as an indicator for monitoring localized fossil fuel CO2 emissions (Miyazaki and Bowman, 2023).

In 2020, the implementation of COVID-19 social distancing policies in multiple countries led to a significant decrease in human activities worldwide (de Palma et al., 2022). While the general anticipation was for a reduction in NO2 emissions in many cities due to the decline in anthropogenic activities (Bauwens et al., 2020; Barré et al., 2021; Cooper et al., 2022), the response of O3 and CH4 has been unexpected.

Increased levels of O3 have been observed in northern Europe, China, and South Africa as a consequence of the COVID-19 lockdown, according to sensitivity simulations conducted using the MIROC-CHASER global chemical transport model (Miyazaki et al., 2021). This rise in O3 can be attributed to the general reduction in NOx, which enhances O3 production by reducing NO titration in areas with high levels of NOx pollution or VOC-limited areas (Akimoto and Tanimoto, 2022). Furthermore, meteorological effects have played a significant role in the changes observed in O3 levels between 2020 and the reference year (Ordóñez et al., 2020; Liu et al., 2021). Despite accounting for the influence of weather conditions, significant variations in O3 level estimates have been reported across studies, particularly in European countries (Ordóñez et al., 2020; Grange et al., 2021), and China (Liu et al., 2021; Shi et al., 2021). The presence of sunlight is essential for the O3 generation in response to the decrease in NOx during the lockdown period. As a result, the lack of sunny conditions in specific urban areas at the time of the atmospheric response to NO2 reduction may have led to differing time delays before observable changes in O3 levels occurred (Grange et al., 2021) (Grange et al. 2021).

In 2020, during the COVID-19 pandemic, global CH4 emissions experienced a significant growth rate, which was contrary to the expected decrease in anthropogenic CH4 emissions due to the implementation of lockdown measures (Peng et al., 2022). In 2020, anthropogenic CH4 emissions only slightly decreased compared to 2019, while wetland emissions rose sharply. This increase in wetland emissions was likely influenced by unusually warm and wet weather in the Northern Hemisphere (Peng et al., 2022), which could be connected to the impact of climate change (Zhang et al., 2023). Apart from the variation in CH4 emission itself, it was found that the decrease in hydroxyl radical (OH) concentration due to changes in air pollutants like NOx, CO, and NMVOCs during the COVID-19 pandemic mainly accounted for approximately half ($53 \pm 10\%$) of the observed global CH4 level growth in 2020 (Peng et al., 2022). A similar finding regarding the effect of NOx, CO, and NMVOCs emission changes on the 2020 methane levels is reported by (Stevenson et al., 2022). However, other studies using Greenhouse gases Observing SATellite (GOSAT) observations indicated that most of observed increase in atmospheric CH4 during 2020 and 2021 can be attributed to increased CH4 emission itself (Qu et al., 2022; Feng et al., 2023). Although CH4 has a long estimated lifetime of 8-10 years and has mostly been discussed at the global level, it is important to note that policies and approaches to address CH4 emissions may vary locally.

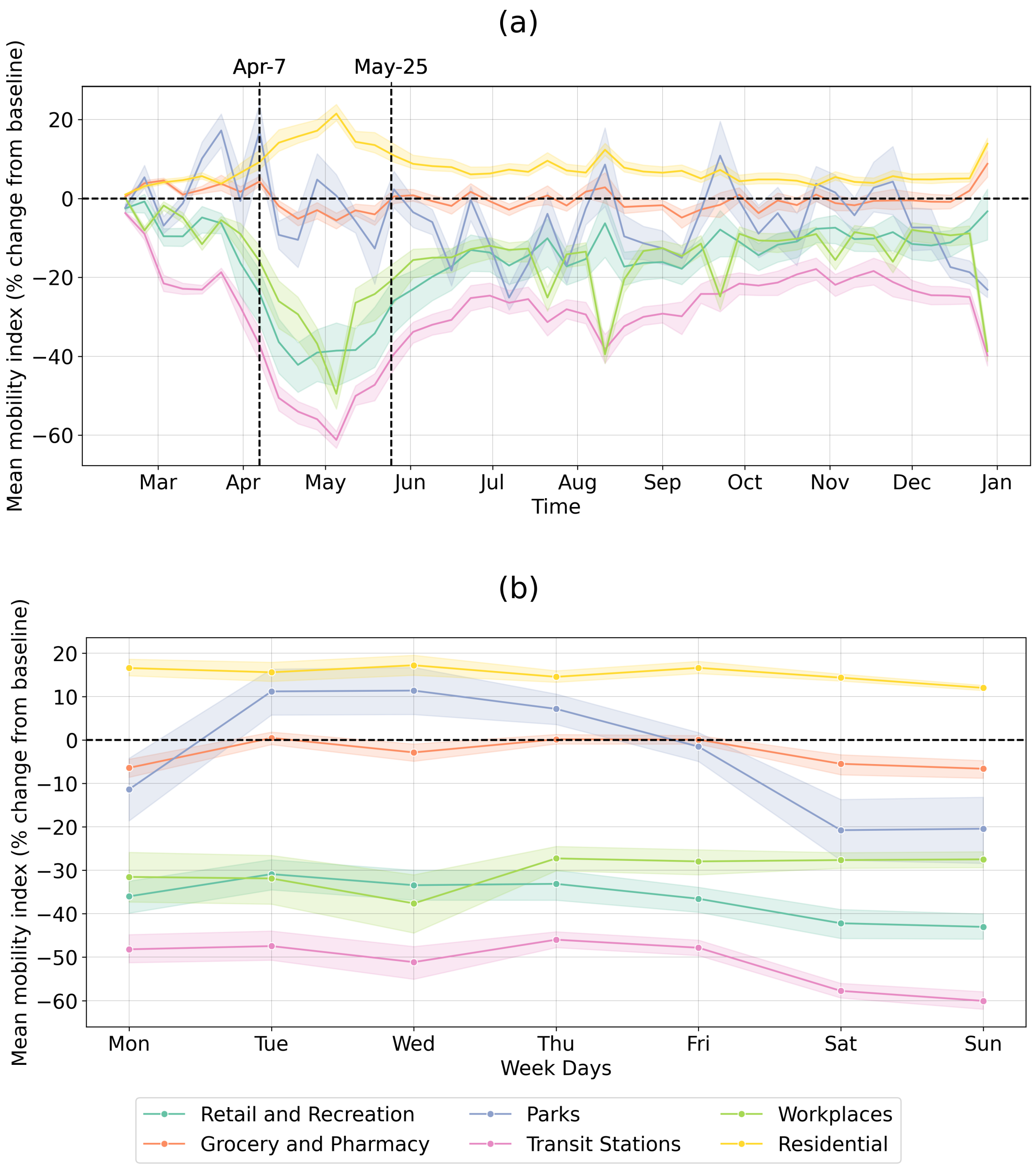

Figure 4.1. Mobility changes for 6 prefectures in Japan (Aichi, Fukuoka, Tokyo, Osaka, Kyoto, and Hyogo) in 2020 based on Google's mobility indices for time-series (a) and days of the week (b)

In 2020, Japan also experienced the impact of the COVID-19 pandemic, and in response to prevent the virus's spread, a state of emergency was declared from April 7 to May 25. This measure resulted in the suspension of various economic activities and imposed restrictions on people's mobility. As a consequence, there was a significant decline (Figure 1) in a unique weekend movement trend (Damiani et al., 2022).

Although the primary aim of the lockdown was not specifically to address air pollution and greenhouse gas emissions, the implementation of these measures offers valuable insights for atmospheric modelling. It provides practical knowledge and first-hand experience to develop more efficient strategies for mitigating air pollution and reducing greenhouse gas emissions in the future (Grange et al., 2021). It is important to note that the changes in air pollutants during this period varied across regions and were strongly influenced by meteorological conditions. Performing a regional analysis of these changes can provide evidence to support the formulation of appropriate regional policies in the future. In this study, our objective is to evaluate the impact of changes in anthropogenic activities during the COVID-19 pandemic (from April 7 to December 31) on NO2, O3, CO and CH4 in metropolitan areas (MAs) of Japan in 2020, which have not been thoroughly investigated in previous studies.

In the first phase (Section 4.2), we gathered data from ground observations, satellite sources, and biogeochemical model simulations. Subsequently, we constructed a weather normalization model under business-as-usual (BAU) conditions utilizing machine learning techniques, incorporating meteorological, spatial, and temporal predictors (Section 4.3). We investigated variations in air pollution levels by analysing the BAU predictions alongside additional data in Section 4.4. Lastly, we provided discussions in Section 4.5, while in Section 4.6, we present our study's findings, conclusions, and recommendations for future policy considerations.

4.2 Data

4.2.1 Study area

Prior research primarily focused on assessing the impact of pandemic lockdown measures on air quality within the Greater Tokyo Area, being the most densely populated metropolitan area globally (Damiani et al., 2022; Zoran et al., 2023). Nevertheless, there's a notable absence of similar analyses for other MAs. Our study covers 14 MAs in Japan, extending from Sapporo in the north to Kagoshima in the south, as depicted in Figure 2. We focus on these metropolitan areas due to their housing of Japan's highly populated and vibrant cities, which are intricately connected with human activities and air pollution in Japan.

4.2.2 Ground observation

To acquire air quality data, we gathered ground observations for NO2, O3, CO, and CH4 from the air quality monitoring data archive published by the National Institute for Environmental Studies (NIES). These observations spanned a ten-year period from 2010 to 2020 and were collected from 1,180 stations for NO2, 835 stations for O3, 383 stations for CH4, and 237 stations for CO. The study utilized two types of stations: roadside air monitoring stations (RsAMS), which are placed in areas prone to air pollution from vehicle exhaust caused by traffic congestion, like intersections, roads, and near road edges, and ambient air monitoring stations (AAMS), which are established to assess air pollution in general living spaces such as residential areas. These station types have been categorized by NIES, and the data can be readily acquired from the original downloadable dataset.

Apart from air quality data, we incorporated ground observations of meteorological data from Japan Meteorological Agency (JMA) as input features for the BAU models used in the study. Specifically, we obtained daily records from 52 weather stations located within the same 14 MAs. At each weather station, we gathered temperature, wind direction and speed, local atmospheric pressure, and relative humidity, as suggested by (Grange et al., 2021). The corresponding meteorological parameters were extracted from the nearest weather observation site for each air quality station.

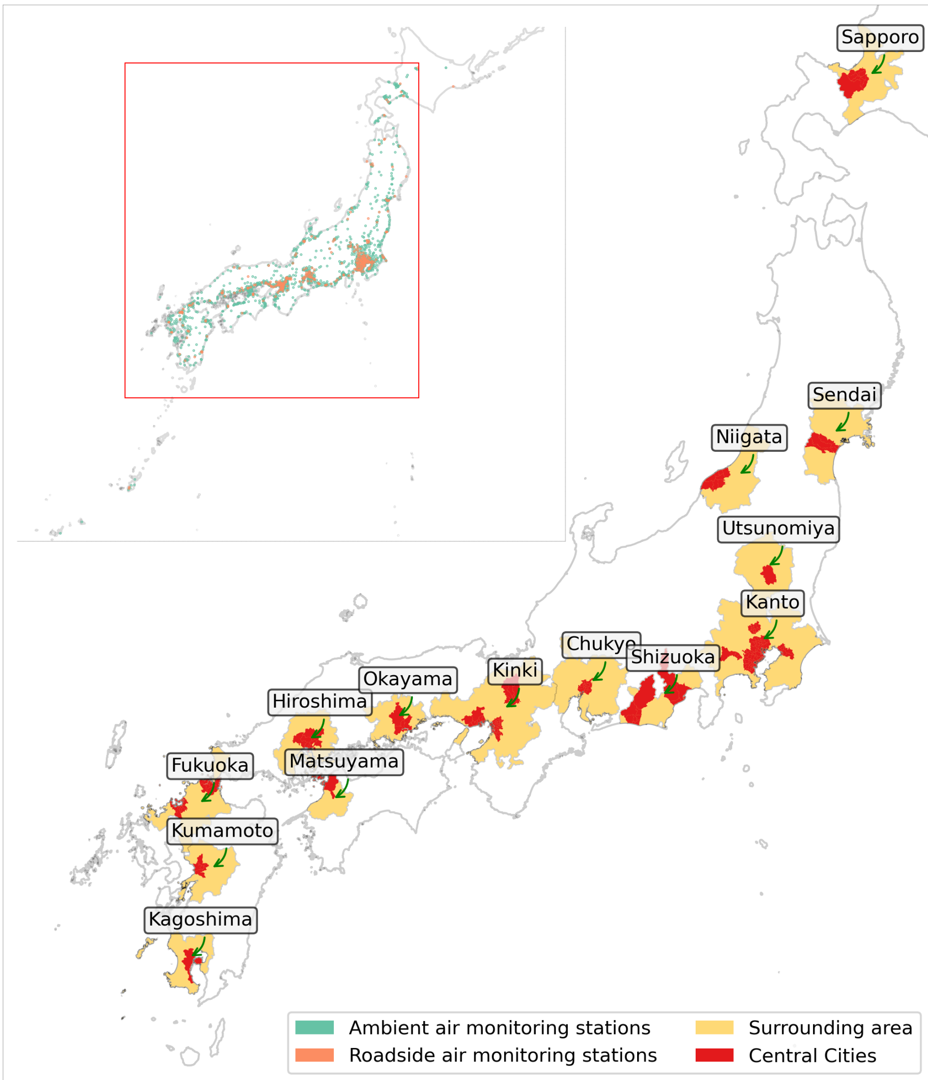

Figure 4.2. The locations of 14 metropolitans' areas and the distribution of ground observations for air quality monitoring in Japan

4.2.3 ERA5 reanalysis dataset

Alongside the weather data collected from the ground stations in the NIES database, for the features of the BAU models, we incorporated additional daily data pertaining to boundary layer height, total cloud cover, downward solar radiation (SR), and total precipitation, as recommended by (Shi et al., 2021). This supplementary information was sourced from the ERA5 reanalysis dataset (ERA5 hourly data on single levels from 1940 to the present) obtained from the Climate Data Store of the Copernicus Climate Change Service. Additionlly, the ERA5 2m temperature variable (T2M) and SR will be utilized to assess the variation of sunny conditions during both the lockdown and post-lockdown periods within the study area. The original ERA5 data possesses a spatial resolution of $0.25° \times 0.25°$.

4.2.4 Sentinel 5P TROPOMI

In this study, we utilized the Sentinel 5P (S5P) Tropospheric Monitoring Instrument (TROPOMI) data to evaluate the tropospheric formaldehyde-to-NO2 ratio (FNR) specifically for the year 2020. This ratio serves as a key indicator for the sensitivity of tropospheric ozone production. The tropospheric NO2 and formaldehyde (HCHO – as a proxy for NMVOCs) data was obtained from the S5P L3 product "OFFL/L3_NO2" (based on processor version 1.2.x and 1.3.x) and "OFFL/L3_HCHO" (based on processor version 1.1.x) collections from Google Earth Engine, respectively. To generate the comprehensive L3 S5P product, each operational level (L2) product underwent preprocessing and mosaicking using the harpconvert tool. The low-quality pixels was filtered out in L3 NO2 product by excluding those with AQ (Air Quality) values below 75% for the band "tropospheric_NO2_column_number_density". The resulting data, ready for download, is available with a spatial resolution of about 1×1 km2.

4.2.5 Biogeochemical modelled CH4 budget

In our assessment of CH4 emission variations, with a specific focus on emissions from natural sources such as wetlands, we utilized CH4 budget data obtained from the Vegetation Integrative SImulator for Trace gases (VISIT) (Ito et al., 2019). VISIT is a biogeochemical model that takes into account historical land use and climatic conditions to estimate CH4 emissions (Ito et al., 2019). The CH4 budgets generated by the VISIT model are now available and accessible through the Global Environmental Database provided by NIES, Japan (Ito et al., 2019). We utilized the global data versions "Ver.2021.1_CH4Wetl_Cao" (Ito, 2021a), and "Ver.2021.1_CH4Wetl_WH" (Ito, 2021b), which incorporate Cao scheme (Cao et al., 1996), and Walter and Heimann scheme (WH scheme) (Walter and Heimann, 2000), to estimate CH4 emission for each MA, which offers CH4 emission information at a spatial resolution of $0.5° \times 0.5°$.

4.3 Method

4.3.1 Business-as-usual (BAU) modelling

To accurately quantify the actual change in the levels of the four pollutants, we developed a weather normalization model under BAU conditions using machine learning. This model was specifically designed to simulate pollutant levels without the influence of COVID-19 restriction measures, using meteorological, spatial, and temporal features as inputs. The meteorological predictors utilized in our model include ground observation data such as temperature, wind direction and speed, local atmospheric pressure, and relative humidity. Additionally, we incorporated data from the ERA5 reanalysis dataset, which comprises boundary layer height, total cloud cover, downward solar radiation, and total precipitation. Temporal predictors included the Julian date (the number of days since January 1) and the day of the week. Furthermore, latitude and longitude coordinates of each station were utilized as spatial predictors. To develop the weather normalization models for each pollutant at both AAMS and RsAMS, we utilized data from the years 2016 to 2019, which offers a comprehensive timeframe to account for the diverse air pollution concentration fluctuations experienced across various meteorological conditions. Extending the period, such as from 2010 to 2019, would not accurately represent recent air quality trends due to the impact of past air pollution reduction policies. Conversely, a shorter timeframe, such as the pre-lockdown period months would not adequately capture the full range of meteorological variations. Overall, four separate weather normalization models were developed for each pollutant (NO2, O3, CO, and CH4), taking into account the specific station type (RsAMS and AAMS).

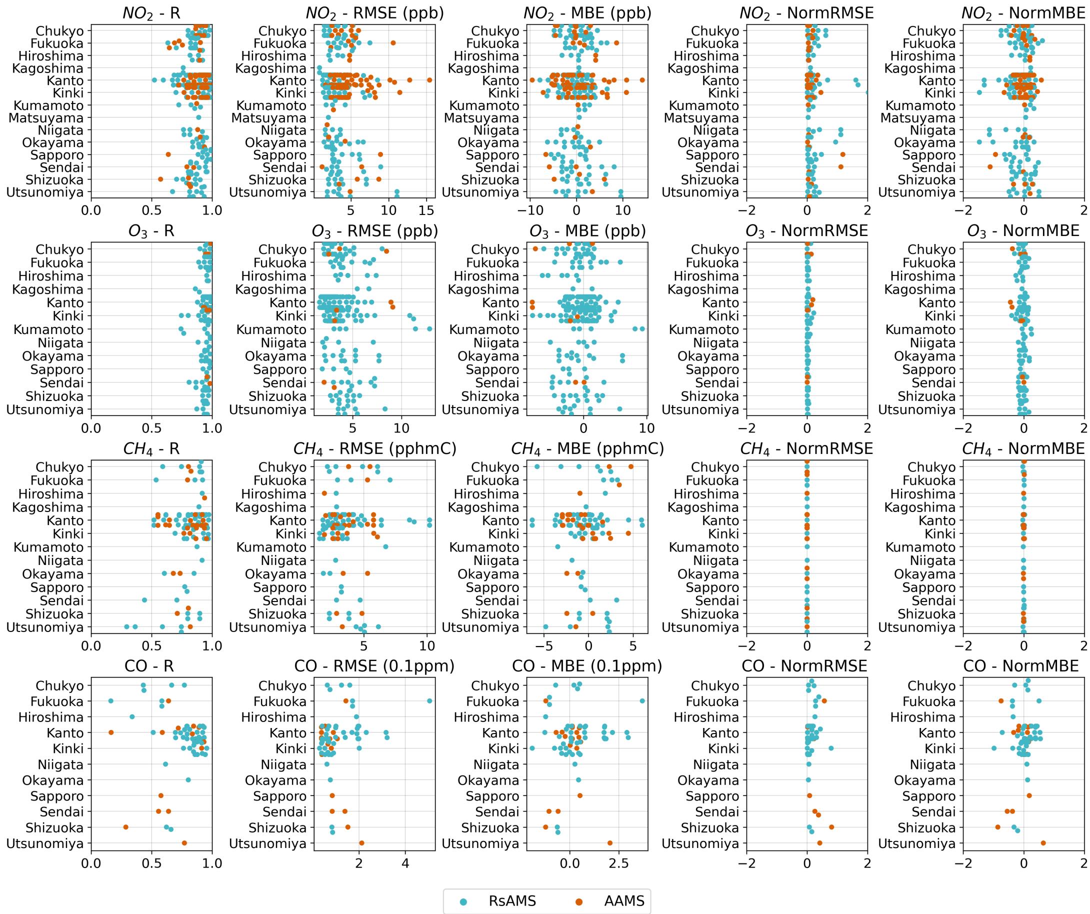

Figure 4.3. The details score of each station on the test set. For each station on the test set, we calculated the following scores and display it in this figure: Pearson correlation coefficient (R), root mean square error (RMSE), normalized root mean square error (NormRMSE) and mean bias error (MBE), normalized mean bias error (NormMBE)

We employed the LightGBM machine learning model (Ke et al., 2017), a gradient boosting decision tree algorithm, to construct the BAU model using the aforementioned predictors. To fine-tune the model's hyperparameters, we utilized Fast and Lightweight AutoML Library (FLAML) (Wang et al., 2021), a

Table 4.1. The performance of BAU model on the test set (30% station data) with the following metrics: Pearson correlation coefficient (R), root mean square error (RMSE), normalized root mean square error (NormRMSE) and mean bias error (MBE), normalized mean bias error (NormMBE). For the normalized MBE and RMSE, we normalize values for each station and then compute the mean

Pollutants	Station type	R	RMSE	NormRMSE	MBE	NormMBE
NO2	AAMS	0.89	3.13	0.15	-0.12	-0.07
	RsAMS	0.88	4.84	0.10	0.30	-0.03
O3	AAMS	0.96	3.75	0.02	-0.37	-0.02
	RsAMS	0.96	4.92	0.06	-3.18	-0.16
CO	AAMS	0.73	0.84	0.17	0.00	-0.07
	RsAMS	0.77	1.23	0.13	0.39	0.04
CH4	AAMS	0.82	3.75	0.00	-0.29	0.00
	RsAMS	0.80	3.82	0.00	-0.26	0.00

lightweight library specifically designed for accurately identifying optimal hyperparameters for models. During the training process, we utilized 70% of the station data within each metropolitan area (MA), while the remaining 30% was reserved for validating the model's performance. Both the training and test data sets were randomly selected for each MA, ensuring unbiased representation across the dataset.

In order to evaluate the performance of the BAU model we utilized the following metrics mean bias error (MBE), normalized mean bias error (NormMBE), root mean square error (RMSE), normalized root mean square error (NormRMSE) and Pearson correlation coefficient (R) as suggested by (Grange et al., 2021). The detailed results are presented in Figure 3 for each pollutant and station, average scores are shown in Table 1. In general, the model demonstrated strong performance with high R values (mostly $R > 0.8$) and low MBE and RMSE scores when applied to the test set for NO2, O3, and CH4. Regarding CO, the model achieved a satisfactory R value ($R > 0.73$).

4.3.2 Experiments design

Our aim is to assess the alterations in NO2 levels within 14 MAs during both the lockdown and post-lockdown periods in 2020. We also intend to explore how changes in NO2 may influence the shifts in O3 and CH4 levels in each of these timeframes. Notably, we were encouraged to undertake this investigation by an observation of an unusual O3 response to NO2 reduction in the Greater Tokyo Area (Damiani et al., 2022), prompting me to study the response of O3 and CH4 in all 14 MAs across Japan.

We conducted three experiments to assess the impact of NO2 changes on O3 and CH4 levels. In the first experiment, we focused solely on quantifying the change in NO2 levels using the time series observations and "OBS-BAU" estimate which involved subtracting the BAU prediction from the observed data (OBS). In the second experiment, we expanded the analysis to include O3, incorporating additional variables from the ERA5 (temperature – T2M and SR) and S5P datasets (FNR and HCHO). The last experiment included CH4, incorporating the "OBS-BAU" estimate for CH4 and NO2, as well as the "OBS-BAU" estimate for CO and simulated CH4 emissions from wetlands using the VISIT model.

For the experiments, we selected April 7 to May 25 as the lockdown period, August 1—31 as the post-lockdown period for O3 analysis, and June 1 to December 31 for CH4 analysis. We selected these timeframes to better understand how the four air pollutants changed in response to the unforeseen COVID-19 lockdown measures and the period after the lockdown.

4.4 Results

4.4.1 NO2 level changes

We initially examined the monthly trend of observed NO2 concentration levels across 1,180 stations in the 14 MAs from 2010 to 2019, and we compared these trends with the NO2 levels observed during the lockdown in 2020 as depicted in Figure 4a. The results indicate that the actual reduction in NO2 levels during the lockdown in 2020 is lower than the trend observed during 2010-2019, specifically 2.7 ppb for RsAMS and 2.2 ppb for AAMS. This implies that the NO2 levels observed during the lockdown were equivalent to those in 2023 for RsAMS and 2025 for AAMS, based on the trend observed during 2010-2019.

Prior studies have indicated the importance of considering meteorological factors when evaluating the effects of intervention measures (Ordóñez et al., 2020; Grange et al., 2021; Shi et al., 2021). In order to accurately assess the impact of the lockdown while isolating the effects of weather conditions, we computed the "OBS-BAU" estimates for all MAs as depicted in Figure 4b. Additionally, Figure 4c presents the complete time series of NO2 levels in 2020 (OBS), the expected levels without the lockdown (BAU), and the average data from 2016-2019 for four MAs (Kanto, Kinki, Chukyo, Fukuoka). We only show the figures for four MAs to avoid overwhelming complexity and to provide a more manageable representation of the figures.

Table 4.2. OBS-BAU estimates for NO2 during the lockdown (April 7 to May 25) and post-lockdown (August 1 to 31). For timeseries estimate, we considered all days of the week. However, when considering weekday, we only included Monday to Friday, while for weekends, we only accounted for Sunday and Saturday. The values are represented as mean (standard deviation)

Station type	Lockdown (April 7 −May 25)			Post-lockdown (August 1−31)		
	Timeseries (%)	Weekday (%)	Weekend (%)	Timeseries (%)	Weekday (%)	Weekend (%)
AAMS	-14.5 (12.1)	-12.9 (14.3)	-18.4 (8.6)	-10.2 (7.3)	-6.8 (7.8)	-17.2 (8.3)
RsAMS	-19.1 (13.5)	-18.0 (14.2)	-21.9 (13.9)	-18.1 (11.2)	-13.6 (12.3)	-27.4 (10.0)

Overall, NO2 levels exhibited a decline across most MAs. The decline in emissions was particularly significant in RsAMS compared to AAMS in most MAs, with an average reduction of 19.1% and 14.5% respectively. However, these reductions were smaller compared to those observed in European cities (Barré et al., 2021; Grange et al., 2021). Additionally, we observed that the reduction in NO2 levels during weekends was more significant than on weekdays, primarily due to a substantial decrease in mobility during weekends compared to weekdays (refer to Figure 1b). During the lockdown the average reduction in NO2 levels for AAMS was 12.9% on weekdays and 18.4% on weekends. As for RsAMS, the average reduction stood at 18% on weekdays and 21.9% on weekends. For most MAs,

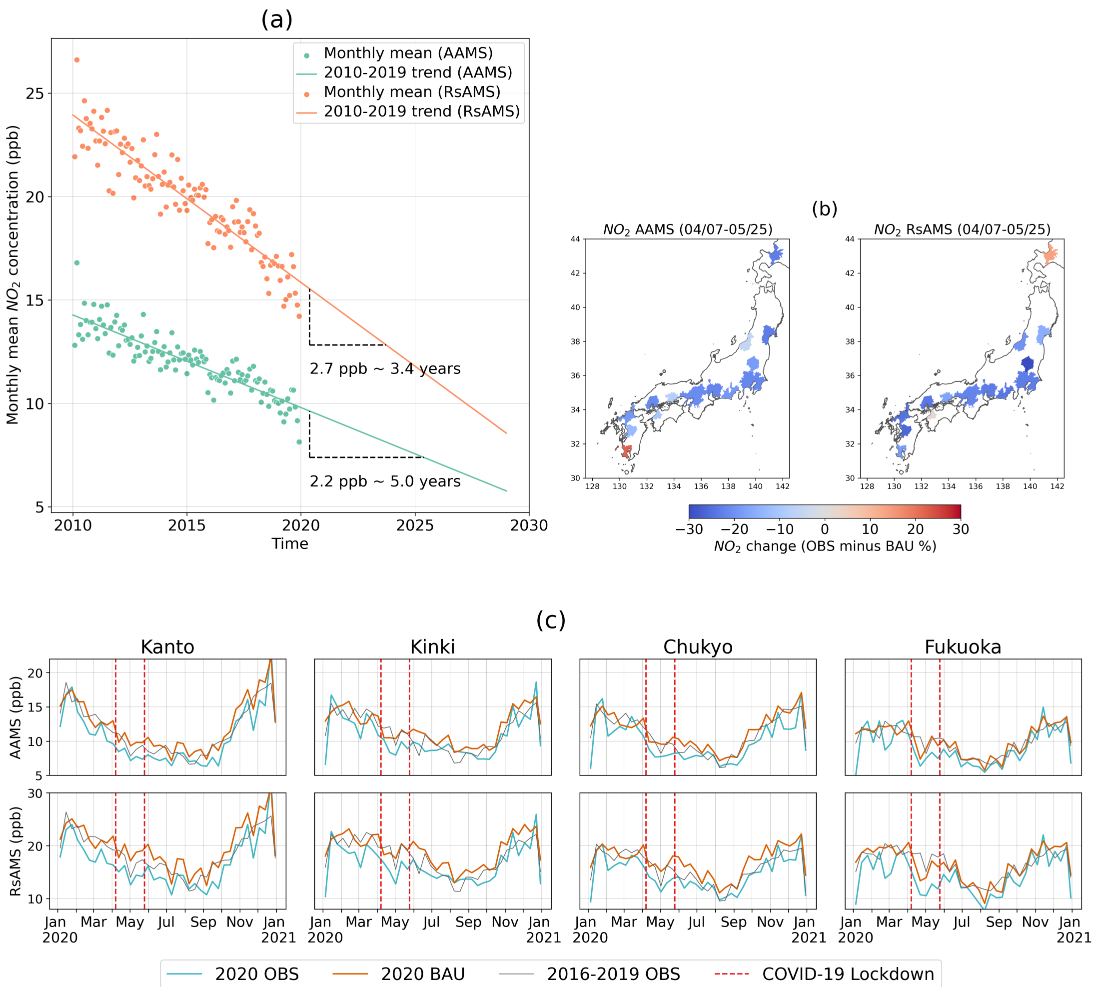

Figure 4.4. (a) Mean ground observation trend with the reduction in NO2 due to the lockdown in 2020 for AAMS and RsAMS. (b) Map visualization of the "OBS-BAU" estimate for NO2 during the lockdown period. (c) The 7-day rolling mean of 2020 observation (OBS), BAU prediction (BAU), and mean level of NO2 from 2016 to 2019 for 4 MAs

even the lockdown has been lifted in the end of May 2020, the NO2 level still continue to decline until the end of December 2020. This ongoing decrease may be attributed to the sustained reduction in mobility trends from the period of the lockdown through the end of 2020 (as illustrated in Figure 1a). These findings are summarized in Table 2 and Table 3.

4.4.2 O3 level changes

In this experiment, we investigated various parameters to gain a better understanding of the changes in O3 in response to the reduction of NO2 caused by COVID-19 social distancing policies. Alongside the "OBS-BAU" estimates, we examined standardized anomalies of T2M and SR between 2020 and 2016-2019 period, S5P FNR in 2020, and changes in S5P HCHO between 2020 and 2019. These parameters were analyzed for two distinct periods: the lockdown period and the post-lockdown (August 1 −31), 2020.

Changes during the lockdown period

During the lockdown period (April 7 to May 25), we observed a slight change in O3 levels across most MAs (Figure 5 second row and Figure 6). On average, there was a reduction of 2.3% in AAMS and 0.6% in RsAMS, as indicated in Table 2. Although the overall trend showed a decrease, we did find instances of increased O3 levels in certain MAs, particularly in RsAMS such as Kanto (1.6%), Kinki (2.2 %), and Fukuoka (3.5 %), as depicted in Figure 5 (second row). Moreover, we have observed the existence of an "ozone weekend effect" in the changes of O3 levels, indicating higher increase in O3 mixing ratios during weekends in comparison to weekdays (Akimoto and Tanimoto 2022). This effect was observed in the "OBS-BAU" estimates for RsAMS in Fukuoka (increased 8.8% - weekends, 1.3% - weekdays) and Kinki (increased 4.9% - weekends, 1.2% - weekdays). The observed slight decrease in O3 levels across most MAs in Japan contrasts with the trends observed in many other major cities worldwide (Shi et al., 2021; Grange et al., 2021), where significant increases in O3 levels have been observed. For instance, after accounting for weather effects, notable increases have been reported in Beijing (28.9 %), Wuhan (44.5 %), Milan (66.8 %) Rome (55.8 %), New York (17.4 %), Los Angeles (14.8 %), and Delhi (26.2 %) by (Shi et al., 2021).

To explore this variation further, we analyzed the disparity in T2M and SR between the corresponding period of 2020 and the reference period 2016-2019 as shown in Figure 5 (3rd row). We observed small positive SR anomalies in the southeast region of Japan and negative SR anomalies in the northeast region. Additionally, across the entire country, negative T2M anomalies were observed. The presence of negative T2M anomalies and fluctuating SR levels suggests that the prevailing weather conditions during this period impeded the production of O3.

Table 4.3. OBS-BAU estimates for O3 during the lockdown (April 7 to May 25) and post-lockdown (August 1 to 31). For timeseries estimate, we considered all days of the week. However, when considering weekday, we only included Monday to Friday, while for weekends, we only accounted for Sunday and Saturday. The values are represented as mean (standard deviation)

Station type	Lockdown (April 7 −May 25)			Post-lockdown (August 1−31)		
	Timeseries (%)	Weekday (%)	Weekend (%)	Timeseries (%)	Weekday (%)	Weekend (%)
AAMS	-2.3 (2.7)	-2.7 (3.2)	-1.2 (2.7)	2.2 (15.6)	3.2 (15.3)	0.0 (18.8)
RsAMS	-0.6 (2.7)	-1.4 (2.7)	1.4 (3.7)	8.9 (10.7)	8.9 (12.3)	8.6 (12.7)

Changes during the August, 2020

In August 2020, the NO2 levels continued to decline in all MAs, albeit at a slower rate compared to the lockdown period, as shown in Table 2. However, during this period, we observed a more noticeable increase in O3 levels across most MAs compared to the lockdown. On average, there was a 8.9% increase for RsAMS and a 2.2% increase for AAMS. Notably, the increase in O3 levels during weekends was more significant than on weekdays in Niigata, Okayama, Kinki and Sendai. Specifically, For AAMS of Niigata, O3 levels experienced a 9.4% increase on weekends and a 5.8% increase on weekdays. In RsAMS of Okayama, O3 levels saw a 13% increase on weekends, exceeding the 10.6% increase observed on weekdays. Similarly, in AAMS in the Kinki region, O3 levels exhibited a weekend increase of 19.8%, surpassing the 17.4% increase observed on weekdays. In Sendai, the increase during weekends was even more pronounced, with a 15.6% increase for AAMS and a 22% increase for RsAMS, whereas on weekdays the increase

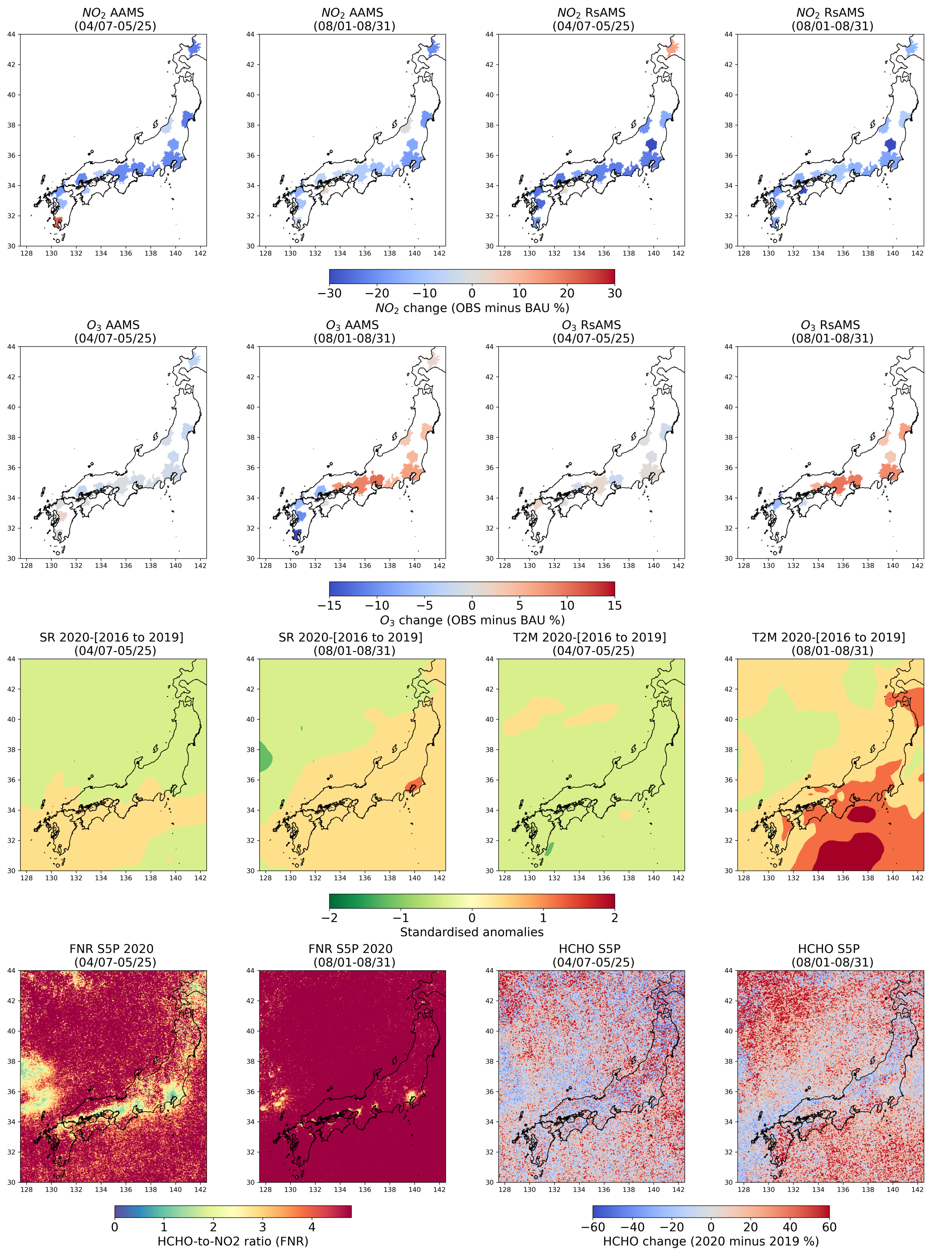

Figure 4.5. The 1st and 3rd columns show the plots for the lockdown (April 7 to May 25). The 2nd and last columns show the plots for August 1 –31. The 1st row: The OBS-BAU estimates of NO2 for AAMS and RsAMS. The 2nd row: The OBS-BAU estimates of O3 for AAMS and RsAMS. The 3rd row: The standardised anomalies of downward solar radiation (SR) and temperature (T2M) from ERA5 dataset. The last row: The formandehyle-to-NO2 (FNR) ratio in 2020 and the HCHO change between 2020 and 2019 from Sentinel 5P data.

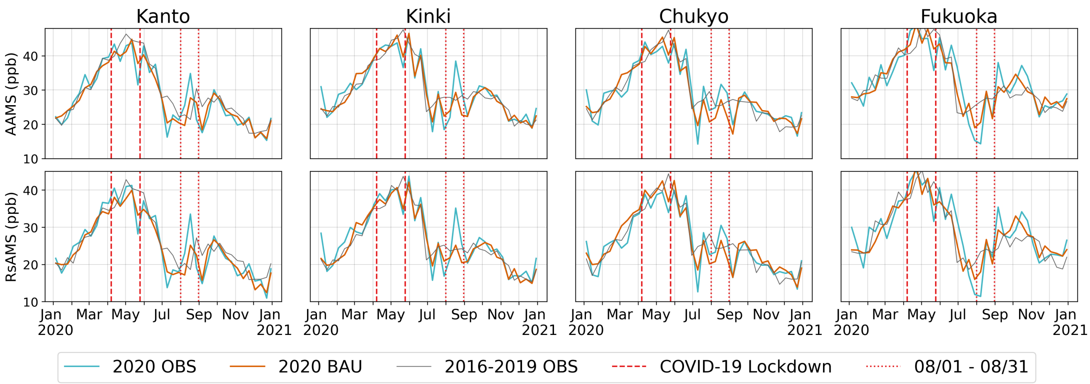

Figure 4.6. The 7-day rolling mean of 2020 observation (OBS), BAU prediction (BAU), and mean level of O3 from 2016 to 2019 for 4 MAs (Kanto, Kinki, Chukyo, and Fukuoka)

was 5.1% for AAMS and 9.8% for RsAMS. This observation could be attributed to the greater reduction in movement during weekends compared to weekdays in these MAs as show in Figure 1b.

In order to investigate the differences in O3 levels between August and the lockdown period, we examined the standard anomalies of SR and T2M in August 2020, comparing them to the 2016-2019 period. Our analysis revealed positive anomalies in both SR and T2M across all MAs, as shown in Figure 5 (3rd row). These favorable weather conditions, combined with the reduced levels of NO2, likely facilitated increased O3 production.

Although there was an overall trend of increasing O3 levels during this period, we did observe a reduction in O3 levels in five MAs which is located in the southern region: Hiroshima (AAMS: 13.7%), Matsuyama (AAMS: 1%, RsAMS: 3%), Fukuoka (AAMS: 12.5%, RsAMS: 12.3%), Kumamoto (AAMS: 20.7%), and Kagoshima (AAMS: 29.9%). To understand the decrease in O3 levels observed in these five MAs, we utilized the S5P FNR for 2020, as well as the changes in HCHO as a proxy for NMVOCs between 2020 and 2019. The FNR is commonly used to assess the sensitivity of near-surface O3 levels (Martin et al., 2004). As suggested by (Duncan et al., 2010), when the FNR is below 1, the O3 production regime is considered VOC-limited, and when it exceeds 2, it is considered NOx-limited. When the FNR values fall within the range of 1—2, O3 is expected to be in the transition regime (Duncan et al., 2010). However, it has been observed that the FNR can vary by region (Jin et al., 2020; Irie et al., 2021; Souri et al., 2023; Ren et al., 2022), and the assumption that it lies within the 1−2 range may not hold true at the global level (Schroeder et al., 2017). Hence, it might be essential to calculate this ratio on a regional scale (Damiani et al., 2022; Schroeder et al., 2017). Despite the FNR showing high variability in the region, it still provides information about the trend of O3 production regimes in our study.

Figure 5 (last row) presents the FNR across all MAs indicating a shift in the O3 production regime from VOC-limited during the initial lockdown to NOx-limited in August. This transition is evident as the FNR changes from $0 < \text{FNR} < 2$ during the lockdown to $\text{FNR} > 4$ in August. During the VOC-limited regime, a decrease in NOx typically leads to an increase in O3 levels (Duncan et al., 2010). However, in the NOx-limited regime, a reduction in NOx can also result in a decrease in O3 levels (Duncan et al., 2010). In Figure 5 (last row), we can observe that the NOx-limited regime dominates the five MAs of Hiroshima, Matsuyama, Fukuoka, Kumamoto, and Kagoshima. Despite NO2 levels continuing to decline during this period, the HCHO levels exhibited a more significant increase in these MAs compared to the lockdown period. Hence, this could explain the reduction in O3 levels observed in these five southern MAs.

We elucidated the difference in O3 levels between major MAs in Japan and other large urban areas worldwide by examining meteorological changes (T2M, SR), and variations in O3 precusors levels by utilizing S5P FNR derived from S5P NO2 and HCHO measurements. The difference can be attributed to the absence of sunny conditions during the lockdown period. However, in August, when sunny conditions became more prevalent, we observed an increase in O3 levels in response to the sustained reduction in NO2 levels across most MAs, which are likely VOC-limited areas. Based on the analysis of S5P data, it appears that the southern metropolitan areas (MAs) exhibited a predominant NOx-limited trend during August 2020, potentially due to the increased presence of biogenic VOCs (BVOCs). However, the monitoring of BVOCs emissions remains challenging due to limited observations (Tani and MOCHIZUKI, 2021; Ito and Ichii, 2021). Therefore, it is also important to pay attention to those NOx-limited areas, as future reductions in anthropogenic NMVOCs may have minimal effectiveness in reducing O3 levels (Akimoto and Tanimoto 2022).

4.4.3 CH4 level changes

In this experiment, we analyze the "OBS-BAU" estimates for NO2, CO, and CH4, and incorporate the VISIT model's simulated CH4 emissions from wetlands to investigate the changes in CH4 levels during the 2020 lockdown and post-lockdown period. Our focus is on understanding the relationship between the reduction in NO2 and its potential impact on OH (hydroxyl radicals), as well as the contrasting effect of CO. The decrease in NO2 levels is expected to result in a reduction in OH, while reductions in CO can increase OH levels and shorten the lifetime of CH4 (Akimoto and Tanimoto, 2022).

During the lockdown period, we observed a marginal rise in CH4 levels across most MAs (Figure 7 third row and Figure 8b), with an average increase of 0.6% for AAMS and 0.8% for RsAMS (Table 3). While NO2 levels decreased in most MAs (Figure 7 first row), the trend for CO varied (Figure 7 second row and Figure 8a). AAMS showed an average decrease of 10.9% in CO levels, while RsAMS saw a slightly smaller reduction 8.8%. Notably, CO levels significantly increased in RsAMS of Kagoshima (60.6%), while slight increases were observed in Kanto AAMS, and in Matsuyama for both RsAMS and AAMS. It is worth noting that although the increases in CO levels in Kagoshima were significant, this region have among the lowest natural CH4 emissions in Japan as Figure 7 (last row), which explains the slight increase in CH4 observed in this MA.

During the post-lockdown period from June to December 2020, NO2 levels continued to decrease, showing an average reduction of 12.8% for AAMS and 18.3% for RsAMS (Table 3) which is smaller than during the lockdown period. In contrast, CO levels started to recover as the COVID-19 lockdown was lifted, with a smaller reduction of 5.7% for AAMS and 5.5% for RsAMS. Notably, significant increases in CO levels were still evident at RsAMS in Kagoshima (62.2%). In Fukuoka we also observed a steady rise of CO levels in both RsAMS (13%) and AAMS (11.5%). In response to these changes in NO2 and CO, we observed a greater increase in CH4 levels during this period, with a rise of 1.3% for AAMS and 1.1% for RsAMS.

In general, we saw a slight increase in CH4 levels both during the lockdown

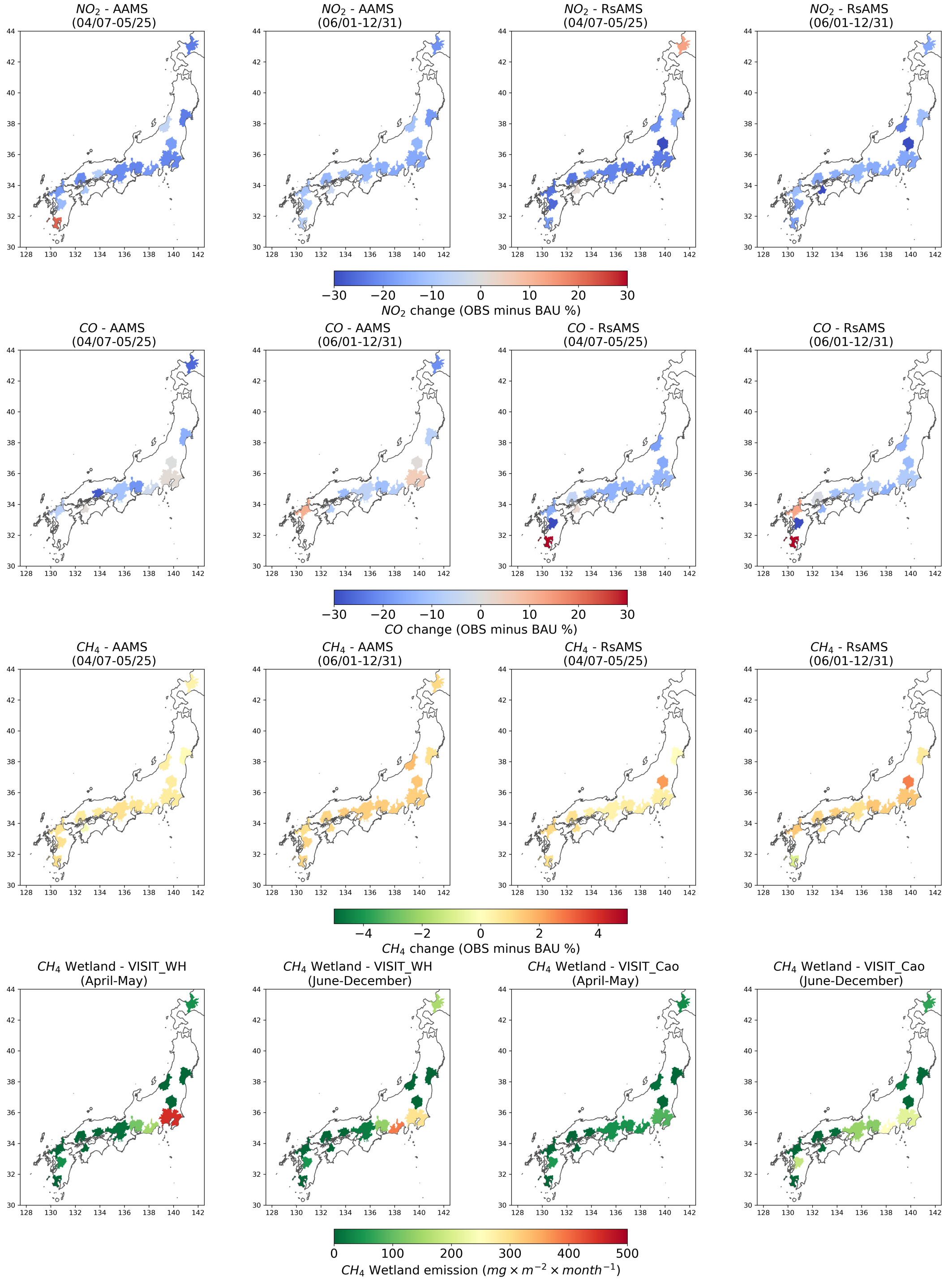

Figure 4.7. The 1st and 3rd columns show the plots for the lockdown (April to May). The 2nd and last columns show the plots for the post-lockdown (June to December). The 1st row: The "OBS-BAU" estimates of NO2 for AAMS and RsAMS. The 2nd row: The "OBS-BAU" estimates of CO for AAMS and RsAMS. The 3rd row: The "OBS-BAU" estimate of CH4 for AAMS and RsAMS. The last row: The CH4 emission from wetland based on the simulation of VISIT model with Walter and Heimann scheme and Cao scheme.

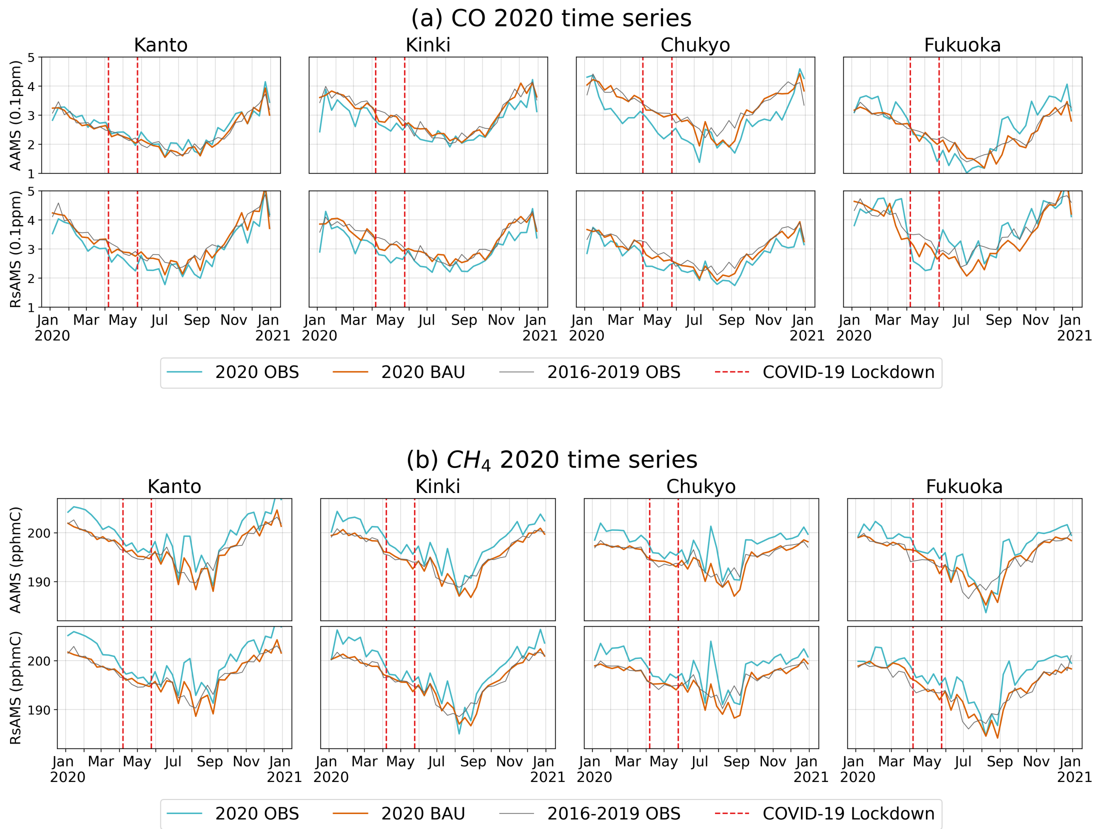

Figure 4.8. The 7-day rolling mean of 2020 observation (OBS), BAU prediction (BAU), and mean level of CO (a) and CH4 (b) from 2016 to 2019 for 4 MAs (Kanto, Kinki, Chukyo, and Fukuoka)

and the post-lockdown periods, based on the "OBS-BAU" estimates. However, a more pronounced increase in CH4 was observed during the post-lockdown phase in AAMS when compared to RsAMS, which can be attributed to the more substantial recovery of CO levels in AAMS relative to the lockdown period. Although it has been reported that global CH4 growth in 2020 is primarily attributed to the atmospheric sink resulting from lower anthropogenic NOx emissions (Stevenson et al., 2022; Peng et al., 2022), our findings regarding the contribution of NOx reduction to the CH4 growth in Japan in 2020 align with a previous study (Akimoto and Tanimoto, 2022; Qu et al., 2022; Feng et al., 2023), indicating that the impact of NOx and CO change on the increase in CH4 growth in Japan during

Table 4.4. OBS-BAU estimates for NO2 and CO and CH4 during the lockdown (April 7 to May 25) and the post-lockdown (June 1 to December 31). For CH4 analysis we only consider timeseries estimate which include all days of the week. The values are represented as mean (standard deviation)

Pollutant	Station type	(April 7 – May 25) (%)	(June 1 – December 31) (%)
NO2	AAMS	-14.5 (12.1)	-12.8 (4.3)
	RsAMS	-19.1 (13.5)	-18.3 (6.4)
CO	AAMS	-10.9 (11.0)	-5.7 (9.4)
	RsAMS	-8.8 (24.6)	-5.5 (25.2)
CH4	AAMS	0.6 (0.3)	1.3 (0.2)
	RsAMS	0.8 (0.6)	1.1 (0.9)

the lockdown and post-lockdown period is not as significant as the direct CH4 emission itself.

4.5 Discussion

4.5.1 Variations in spatial resolution of multisource data

Since we utilized multisource data for the analysis, we acknowledge that variations in spatial resolution among input data can influence the consistency and reliability of data analysis. In certain situations, the need for interpolation to achieve a uniform grid may arise, particularly when generating inputs for a Convolutional Neural Network (CNN). This interpolation process inadvertently introduces uncertainty into the results. However, in this study, we refrained from any data interpolation and used it at its provided original resolution. The multisource data was employed for two primary objectives: weather-normalization model development and visual examination purpose.

For weather-normalization model development, we used ERA5 data and ground station data to construct the weather-normalization model. Certain variables, such as total cloud cover and boundary layer height, are exclusively available from ERA5. The ERA5 data we employed has a resolution of $0.25° \times 0.25°$, meaning that some stations might share identical ERA5 records. This can influence the model development, even though, ideally, local ERA5 values for each station should be distinct, albeit not significantly deviating from the $0.25° \times 0.25°$ spatial resolution value. To mitigate this effect on the model development, we have integrated spatial context values (latitude and longitude) and station types as additional inputs. Since these features are distinct for each station, we anticipate that they can help minimize the impact of the coarse spatial resolution from ERA5 on the model.

To visually inspect the sensitivity of tropospheric O3 production utilizing S5P HCHO and NO2, as well as CH4 emission estimates from wetland, we rely exclusively on original data with consistent spatial resolution. It's important to note that our primary focus is to visually inspect the prevailing trends at the MA level, which has a spatial resolution coarser than that of any input data we utilized. Therefore, we believe that the dominant trends at the MA level remain unaffected by these spatial disparities in this particular MA-level context.

4.5.2 Limitations

In this research, we utilized the S5P FNR to examine the sensitivity of O3 production. Although HCHO could be an alternative indicator for NMVOCs presence, the significant uncertainty in the FNR threshold from previous studies, along with the lack of NMVOCs observations and reliable satellite HCHO and NO2 data, poses challenges in understanding O3 level variations during and after the lockdown period. This issue is particularly crucial and warrants in-depth exploration in future studies.

Additionally, it's important to mention that the study did not include an analysis of long-range air pollution transportation from China to western MAs of Japan following the Chinese economic recovery from the pandemic (Itahashi et al., 2022). This aspect was beyond the scope of the current research but should be considered in future investigations.

4.6 Conclusion

This study presents an air quality analysis that examines the changes in four air pollutants, namely NO2, O3, CO, and CH4, during the COVID-19 pandemic in 14 MAs of Japan from April 7 to December 31 in 2020. Firstly, we developed a machine learning BAU model that incorporates meteorological, spatial, and temporal features to account for weather variability in air quality time series. Next, we utilized the BAU model predictions and observation data to estimate the actual reduction (OBS-BAU estimate) in NO2 levels. We then integrated temperature and solar radiation anomalies from ERA5 reanalysis data and S5P TROPOMI data (FNR and HCHO) along with the "OBS-BAU" estimate to investigate the unique response of O3 to the NO2 reduction during the lockdown and post-lockdown period (August 1 – 31, 2020). Finally, we evaluated the impact of NO2 and CO changes on the CH4 levels using a combination of "OBS-BAU" estimate and wetland CH4 emission simulations from the VISIT model. The main findings of the study can be summarized as follows:

Based on ground observations of NO2, the reduction of NO2 during the lockdown period in 2020 corresponds to a decrease equivalent to 3.4 years and 5 years of the 2010-2019 trend of NO2 for roadside and ambient air monitoring stations respectively. After normalizing the meteorological effects by BAU predictions, the NO2 reduction was 14.5% for AAMS and 19.1% for RsAMS. The decrease in NO¬2 levels is more pronounced during the weekend than on weekdays.

By analyzing ground observations of NO2 and O3, along with BAU simulations and meteorological data from ERA5, as well as FNR and HCHO data from S5P TROPOMI, we found that the reduction in NO2 levels during the lockdown did not immediately result in an increase in O3. Instead, we observed that the increase in O3 occurred after the lockdown, specifically in August when sunny conditions were reinforced. This finding is significant for Japan, as it has not been previously reported in other studies.

Furthermore, when analyzing the ground observations of NO2, CO, and CH4 alongside BAU simulations and model-simulated CH4 emissions from wetlands, we found that the changes in NO2 and CO contributed marginally to the variations in CH4 levels, ranging from 0.6% to 1.3%, across the study areas. This finding aligns with previous studies (Akimoto and Tanimoto, 2022; Qu et al., 2022; Feng et al., 2023), but also differs from others where the reduction in atmospheric sink has been reported as a major contributor to increased CH4 levels (Stevenson et al., 2022; Peng et al., 2022).

Based on the findings of this study, we recommend simultaneous reduction of air pollutants and anthropogenic VOCs as well as biogenic VOCs to mitigate the adverse effects on O3 and CH4. These pollutants are significant SLCPs that can have detrimental impacts on future climate mitigation efforts. Therefore, it is crucial to address both air pollutants and VOCs emissions to effectively mitigate these adverse effects in the future policies.

GREENHOUSE GAS ESTIMATION, FORECASTING AND MONITORING

5 Plant functional types mapping

We proposed a combined machine learning approach with a deep convolutional neural network (CNN) to monitor forest utilization toward Sustainable Development Goals (SDGs) for data-scarce regions. First, we employed the Random Forest (RF) classifier using Google Earth Engine (GEE) for forest mapping. Then, we designed a deep CNN architecture that works for tree species/age mapping from coarse and polygonal ground-truth data. The proposed network has U-shape and comprises 3D Atrous Convolutions. The model was optimized by a weighted cross-entropy loss function. We trained the model with times-series Sentinel 1, 2, and Digital Elevation Model (DEM) data with sparse annotations. Our proposed models achieved 94.5% overall accuracy (OA) for forest mapping, 77.80% (OA) for tree species, and 81.74% (OA) for tree age classification, respectively in Ena city, Japan. The outcome of our study indicates the potential of remote sensing and machine learning in monitoring forest development, conservation, and utilization toward SDGs from coarse ground-truth data. Our source code for the implementation is available at: `https://github.com/anhp95/forest_attr_segment`

5.1 Introduction

Forest plays an important role in achieving SDG15 and mitigating the climate change at the global level. With the help of remote sensing and state-of-the-art machine learning algorithms, mapping the forest area with tree species/age could contribute to monitoring the forest-related SDG issues such as SDG indicators 15.1.1, 15.2.1, 15.4.2.

Forest mapping is a well-known task in land-cover/ land-use classification problems. However, tree species/age map is obtained at the cost of much higher complexity. In the previous studies in tree species/age classification, either high-resolution input (Schiefer et al., 2020; La Rosa et al., 2021) or ground-truth data (point-level) is commonly used. These materials are considered to be expensive, time-consuming to collect, and rarely available in specific regions (e.g., developing regions). Therefore, in this chapter, we present a methodology to help monitor forest areas, tree species/age from coarse annotations and free remote sensing data. Firstly, we classify forest area using RF classifier. Subsequently, we designed a deep CNN architecture for tree species/age segmentation. We demonstrated that our proposed approach is considered to be useful for data-scarce regions.

The paper outline is described as follows. Section 5.2 presents the study area and data used in the paper. Section 5.3 provides the overall methodology and the experimental results in the study area are introduced in Section 5.4. Finally, the conclusion of the paper and the future works is remarked in Section 5.5.

5.2 Data

5.2.1 Study area

The study area is Ena city, located in the southeastern part of Gifu prefecture, middle of Japan. The total area of Ena city is approximately 504 km2 with an elevation of 282 meters. The annual temperature of the city ranges from 2 °C to around 26.4 °C. According to the statistics of the local government, 60% of the forest in Ena is artificial forest which is dominated by Chamaecyparis obtusa. Here, the forest plays a vital role in timber production, water-related disaster prevention and CO_2 sequestration.

5.2.2 Data collection

For forest mapping, we randomly selected a training set (forest/non-forest: 750/250 points) and a validation set (forest/non-forest: 300/100 points) based on the land-use map in 2016 provided by National Land Information Portal. For tree species/age mapping, we collected the labeled data from the same resource. The ground-truth data is available as coarse polygons each covering a mixed-species zone that was annotated by the most dominant tree species of that area. Only na-

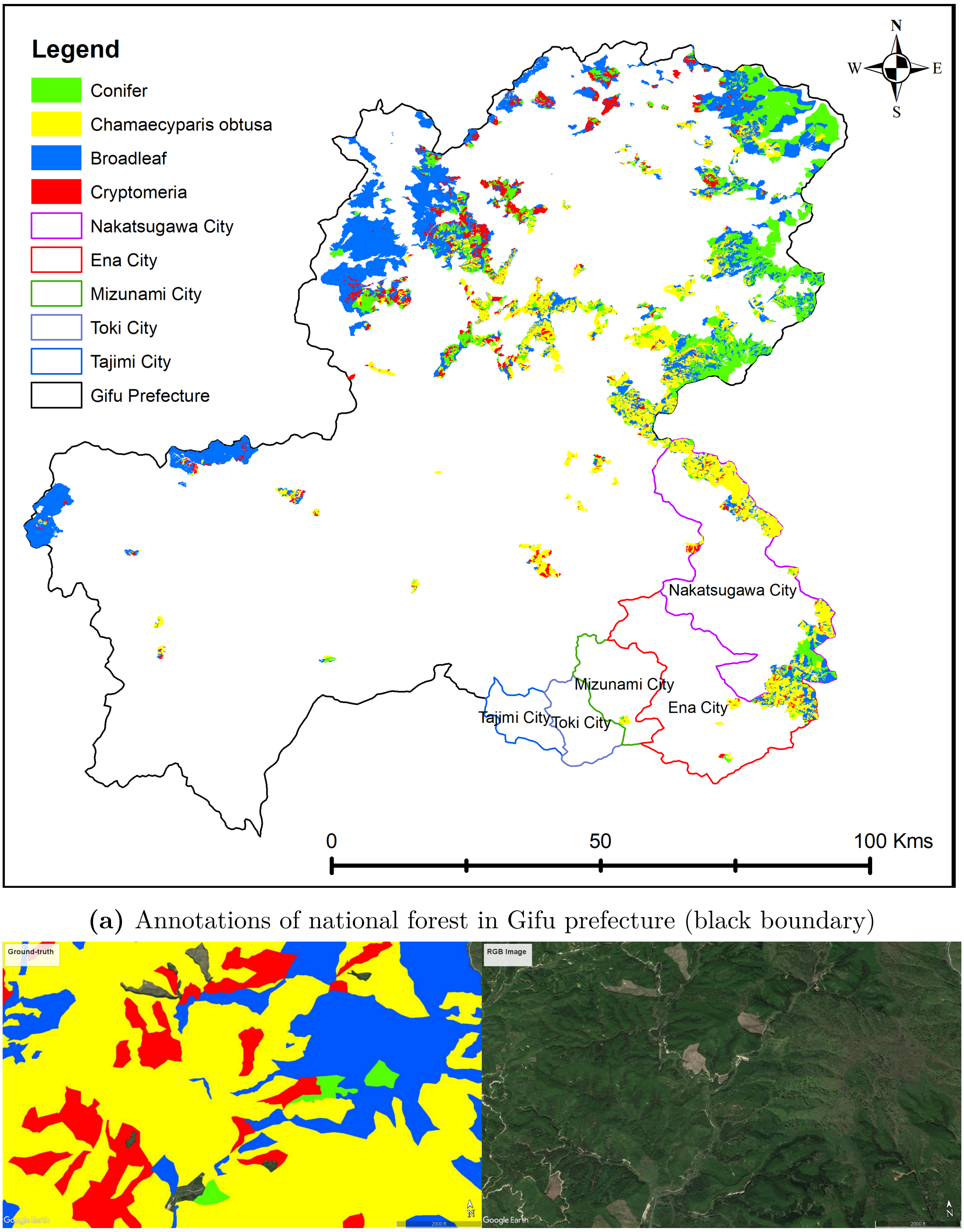

(a) Annotations of national forest in Gifu prefecture (black boundary)

(b) Example of annotated area **(c)** The corresponding RGB image

Figure 5.1. (a) The designated study area outlined in red is Ena city, (b) demonstrates coarse annotations as an illustrative example, and (c) showcases the corresponding RGB image sourced from Google Earth.

tional forest data is available in this database. Due to a small portion of national forest data in Ena city (11%), we utilized the data collected in 2018 from Gifu prefecture to train the model. The remote sensing resource we applied includes Sentinel 1A, Sentinel 2 L1C, and DEM with a spatial resolution of 10m, 10m, and 30m, respectively. The dataset contains 11 spectral channels: Red, Green, Blue, Red Edge, Near-infrared, Short-wave infrared, and Normalized difference vegetation index of Sentinel 2, and VV, VH bands of Sentinel 1A, respectively. The DEM data is NASA Shuttle Radar Topography Mission digital elevation model. The details of the acquisition time of Sentinel 1,2 are described in Section 4.1 and 4.2 for tree species/age segmentation and forest mapping, respectively.

5.3 Methodology

The proposed overall workflow is shown in Fig. 1. First, the Sentinel 1 data was directly downloaded from GEE as each pixel is the backscatter coefficient derived from a chain of preprocessing steps including applying orbit file, GRD border noise removal, thermal noise removal, radiometric calibration, and terrain correction. Sentinel 2 data was mosaicked and monthly average to remove clouds and missing values. The training and validation set for forest mapping; tree species/age segmentation were sampled from the satellite images. In the following sections, we illustrate how the obtained training and validation sets are utilized to train the machine learning models.

Forest mapping

In order to quickly map the forest, we deployed the RF model which is a popular ensemble machine learning classifier for land-cover/land-use classification (Gislason et al., 2006). In addition, RF has been proven to be effective in land-cover mapping from low-resolution ground-truth data (Robinson et al., 2021).

Tree species/age mapping

Although RF is able to perform well with low-resolution labeled data, it is not sufficient to achieve a better result than our proposed deep learning model (Ta-

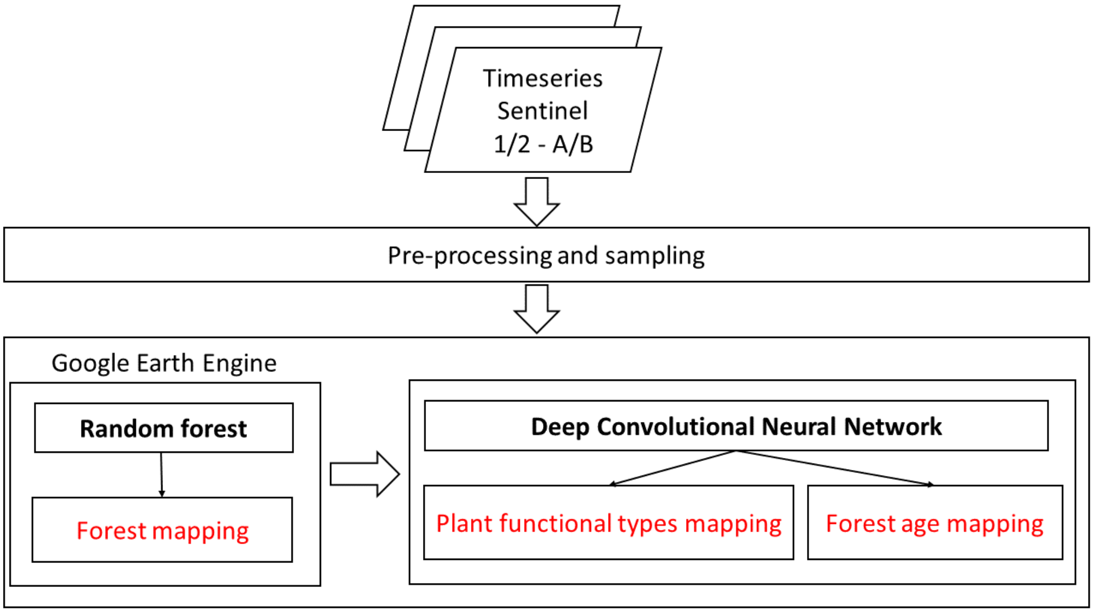

(a) Annotations of national forest in Gifu prefecture (black boundary)

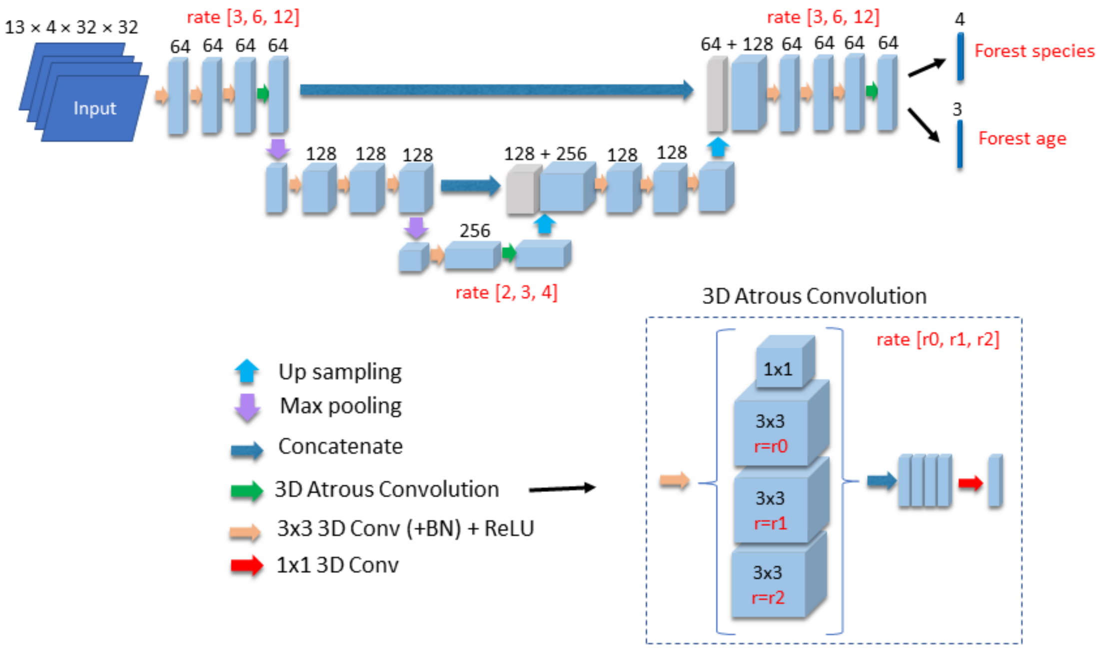

(b) Annotations of national forest in Gifu prefecture (black boundary)

Figure 5.2. (a) The designated study area outlined in red is Ena city, (b) demonstrates coarse annotations as an illustrative example, and (c) showcases the corresponding RGB image sourced from Google Earth.

ble. 2). The proposed network was designed based on the UNET architecture (Ronneberger et al., 2015) and is shallower than the original version (see Fig. 2). We applied 3D Atrous Convolution (3DAConv) to the model as atrous convolution is proven to be effective in semantic segmentation from coarse annotations (Chen et al., 2017b). Atrous convolution was introduced in DeepLab architecture (Chen et al., 2017a) as a term for convolution with upsampled filters. The model backbone is built from encoder and decoder paths. The encoder path consists of three layers. The first one has three 3D convolutions (3DConv) followed by a 3DAConv. The second layer only contains three 3DConvs. The last layer consists of one 3DConv followed by a 3DAConv. A $2\times2\times2$ max pooling layer with strides of two follows each encoder layer. Each 3DConv is followed by a rectified linear unit (ReLU), before each ReLU is a batch normalization (BN). We avoid doubling the number of channels right before the max pooling as introduced in 3D UNET (Çiçek et al., 2016). In the decoder path, the up-convolution (ConvTranspose3D) was applied to upsample the feature map. A 3DAConv was added at the end of decoder path. The output dimensions will be reduced to the number of labels by a $1\times1\times1$ 3DConv from the last 3DAConv. The number of labels in our case is 4 for tree species: Broadleaf, Conifer, Cryptomeria, Chamaecyparis obtusa; 3 for tree age: young age ($\leq$ 20 years), mature age (21-50 years), harvesting age ($\geq$ 50 years).

Table 5.1. Training and validation samples and the corresponding weights for cross-entropy loss function.

Class	Training set	Validation set	Weight
Tree species (number of input images)			
Broadleaf	5017	264	0.153
Conifer	3048	160	0.252
Chamaecyparis obtusa	3191	168	0.241
Cryptomeria	768	40	1
Tree age (number of input images)			
Harvesting age	4000	205	0.05
Mature age	2095	110	0.1
Young age	186	10	1

Experiment design and settings

For tree species/age mapping, we designed the following experiment to evaluate the performance of the proposed network with the RF, 2D, 3D UNET, and our model. The time-series satellite data of Sentinel 1, 2 in 2018 was organized into three periods: January-April (P1), May-August (P2), October-December (P3). For each period, the satellite image was mosaicked and composited. We first investigate the effect of seasonal changes on the performance of tree species/age mapping from satellite data employing RF and 2D UNET. Due to the input shape constraint, we only can examine the performance of 3D UNET and the proposed model with the data of the entire year. In order to train the data with our network or 3D UNET, the input shape must be $13{\times}4{\times}32{\times}32$. In doing so, the DEM band was stacked to the Sentinel 1/2 in P1, P2, P3 (each $13{\times}32{\times}32$) to make the input trainable to the network.

To evaluate the performance of the segmentation models, we used overall accuracy (OA) score on the validation set. Finally, the results map obtained by each model were generated for visual examination.

We implemented the deep learning model in Pytorch and trained the model on NDVIA GeForce RTX 3080 Ti GPU. The model was trained with 100 epochs and was optimized by Adam optimizer with the initial learning rate 10^{-5}. The learning rate is divided by 2 after every 10 epochs.

For forest mapping, the implementation is directly supported in the GEE API which effortlessly enhances the computing performance for mapping stages.

5.4 Experimental results

For forest mapping, only Sentinel 2 in June 2018 with 10m-resampled DEM data derived from GEE were used to train the RF classifier as by our observation, June data has least slope effect in regions with high elevations. The model achieved 94.5% OA for forest/non-forest classification. The forest map produced by the model is shown in Fig. 3.

As observed from Table. 2, RF outperformed 2D UNET in all the tests. Both RF and 2D UNET experiments had a certain outcome that employed only P2 period resulting in the lowest OA in both species and age segmentation. The

Table 5.2. The experimental results of UNET and our model.

Model	Time-series period	Highest OA (%)	
		Species	Age
RF	P2	67.41	73.94
	P1 + P2	71.68	78.66
	P1 + P2 + P3	71.65	78.68
2D UNET	P2	59.81	65.67
	P1 + P2	67.25	75.4
	P1 + P2 + P3	65.02	74.55
3D UNET	P1 + P2 + P3	76.91	80.53
Our model	P1 + P2 + P3	77.80	81.74

OA is significantly improved when a longer time-series scheme is adopted from P2 to P1 + P2. Adding P3 to the training set did not enhance the performance of RF and 2D UNET compared to P1 + P2. That means, in terms of utilizing time-series data for forest species/age segmentation in the study area, it would be preferable to use the data collected from January to August period with an ensemble learning model from multiple decision trees like RF or a 2D UNET-based CNN architecture.

Despite a minor effect of P3 data to the performance of RF and 2D UNET, with 3D CNN scheme in 3D UNET and our suggested model, incorporating P3 data has essentially increased the OA of tree species/age discrimination. The performance of our model and 2D/3D UNET in 100 epochs is presented in Table. 2, Fig. 4, and Fig. 5. The OA has importantly improved from 71.68% to 76.91% with 3D UNET, 77.80% with our model for tree species segmentation, and from 78.66% to 80.53% with 3D UNET, 81.74% with our model for tree age segmentation.

The OA profiles in Table. 2, Fig. 4, and Fig. 5 show that our model outperformed RF, 2D UNET and 3D UNET by approximately 6.12%, 10.55%, 0.89% OA for tree species and 3.03%, 6.31, 1.18% OA for tree age segmentation, respectively.

Fig. 6 is the tree age map produced by our model. The major harvesting-age

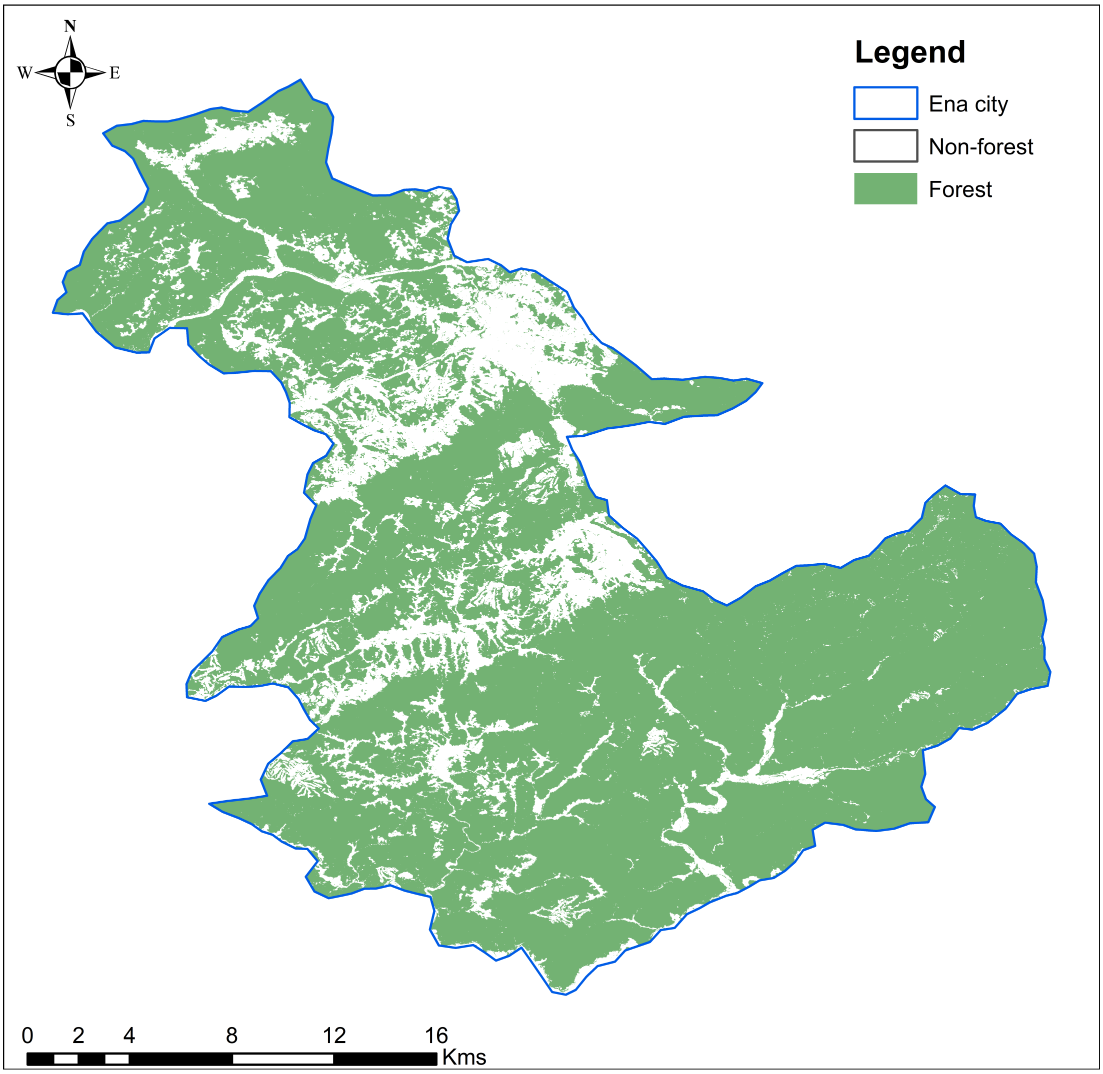

Figure 5.3. Forest map in Ena City, Japan.

area was inferred to be mostly located in the Northern, Southern, and central parts of the city. The major mature-age forest is distributed throughout the region while small areas of young-age forest are observed scattering over the city from the west to the south.

The inferred tree species map is illustrated in Fig. 7. Chamaecyparis obtusa is the most dominant tree and is distributed all over the region. Cryptomeria is predominantly occupied in the central Southeast and Northwest part of the study area. The majority of Broadleaf are mostly allocated in the Northeast,

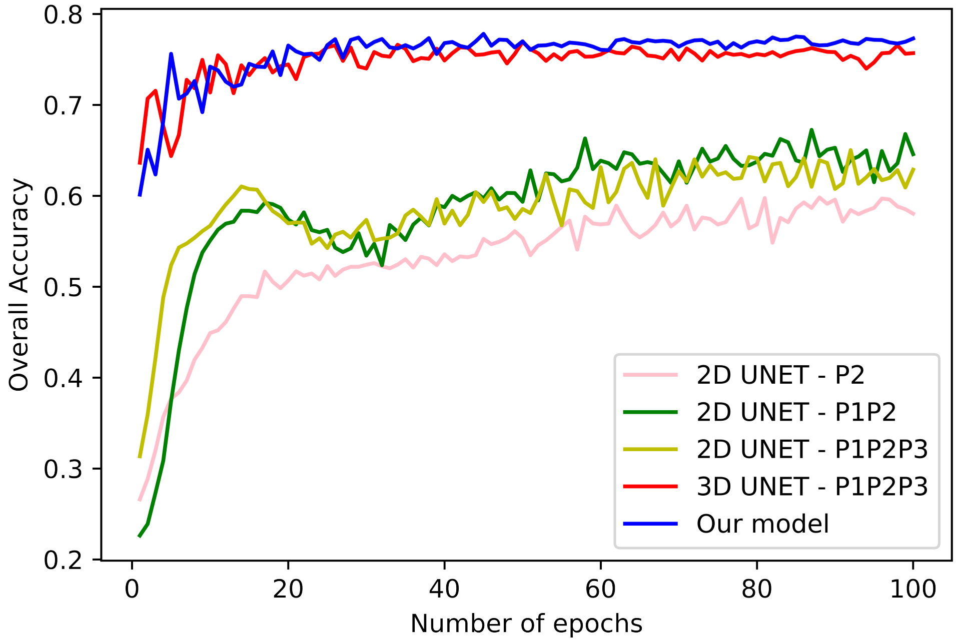

(a) Tree species segmentation.

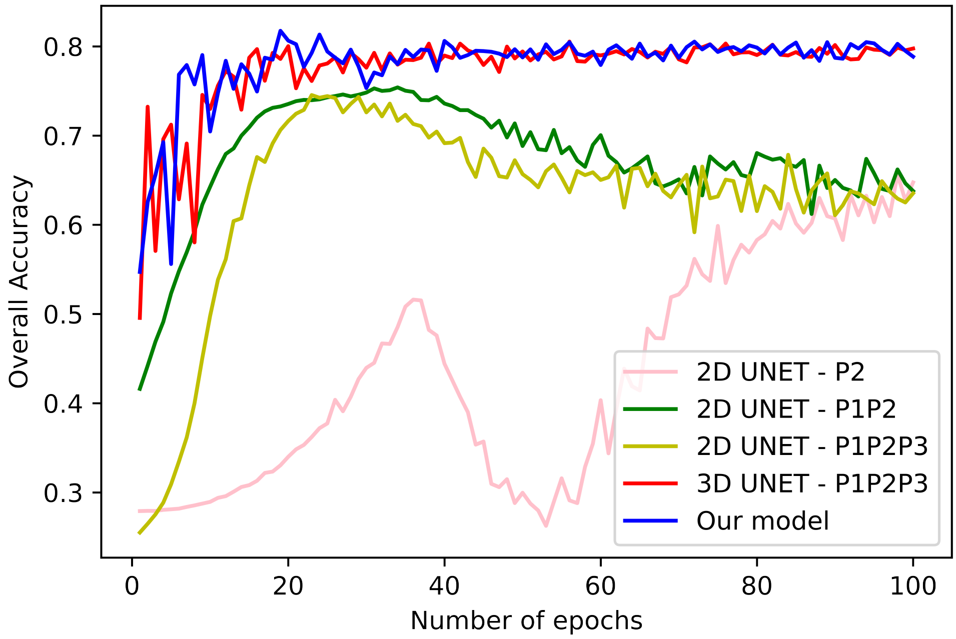

(b) Tree age segmentation.

Figure 5.4. OA profile of tre species (a) and tree age (b) segmentation

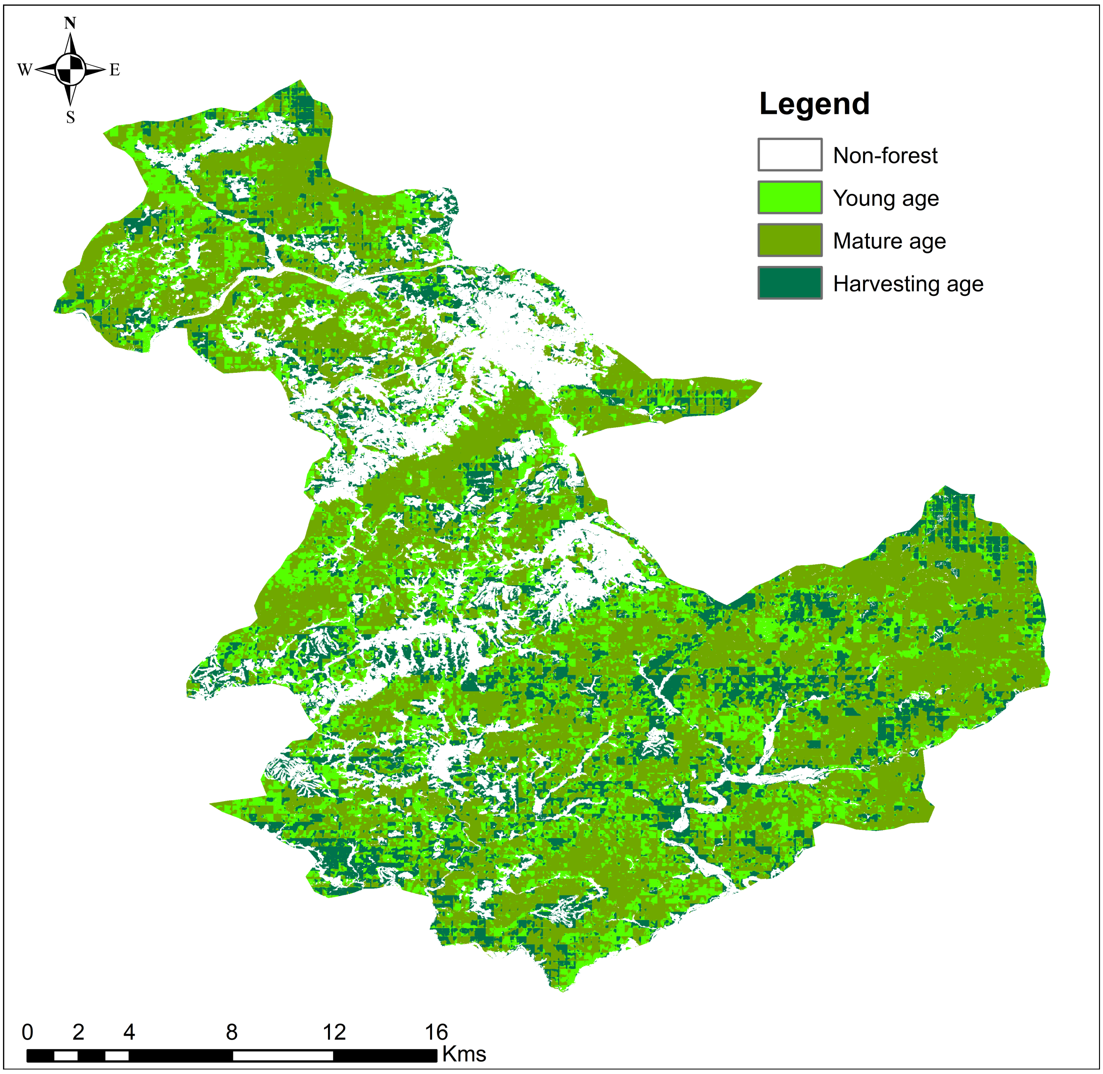

Figure 5.5. Inferred tree age map in Ena City, Japan – 2018.

Southern, and Northwest parts of the region. The detected Conifer is scattered in the area in the Northern and Southern parts, a minor contribution comes from the Northwest of the city

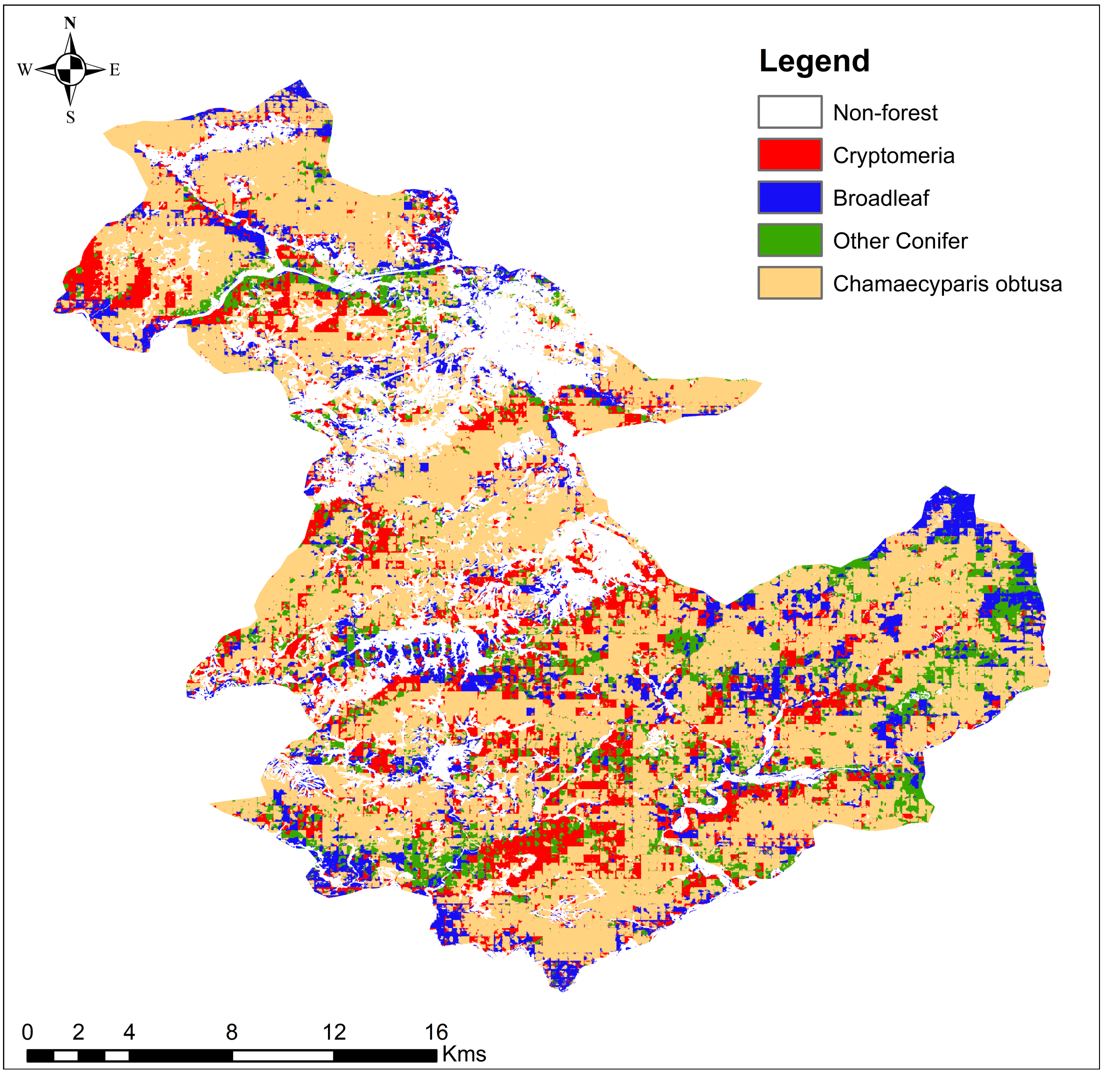

Figure 5.6. Inferred tree species map in Ena City, Japan – 2018.

5.5 Conclusion

In this study, by utilizing remote sensing, RF classifier, and deep learning, the approach for forest-related SDG issues monitoring in data-scarce regions has been proposed. We examined the approach in Ena City, Japan and achieved promising results in forest mapping, and tree species/age mapping. Our proposed model outperforms the RF, 2D/3D UNET in tree species/age segmentation with coarse-polygonal ground-truth data. The outcome of this study could be served as an input for further steps to produce high-resolution land cover map for the data-scarce regions. In the future, we will investigate the postprocessing method to improve the map quality from coarse annotations.

6 Global upscaled of carbon fluxes

7 CO2 monitoring platform

7.1 Introduction

7.2 Method

7.2.1 Data collection

7.2.2 API development

7.3 Result and discussion

7.3.1 Result

7.3.2 Discussion

8 Conclusion

Lorem ipsum dolor sit amet, consectetur adipisicing elit, sed do eiusmod tempor incididunt ut labore et dolore magna aliqua. Ut enim ad minim veniam, quis nostrud exercitation ullamco laboris nisi ut aliquip ex ea commodo consequat. Duis aute irure dolor in reprehenderit in voluptate velit esse cillum dolore eu fugiat nulla pariatur. Excepteur sint occaecat cupidatat non proident, sunt in culpa qui officia deserunt mollit anim id est laborum.

Acknowledgements

Thank you, and thank you.

Bibliography

Hajime Akimoto and Hiroshi Tanimoto. Rethinking of the adverse effects of nox-control on the reduction of methane and tropospheric ozone–challenges toward a denitrified society. *Atmospheric Environment*, 277:119033, 2022.

Jérôme Barré, Hervé Petetin, Augustin Colette, Marc Guevara, Vincent-Henri Peuch, Laurence Rouil, Richard Engelen, Antje Inness, Johannes Flemming, Carlos Pérez García-Pando, et al. Estimating lockdown-induced european no< sub> 2</sub> changes using satellite and surface observations and air quality models. *Atmospheric chemistry and physics*, 21(9):7373–7394, 2021.

M Bauwens, S Compernolle, T Stavrakou, J-F Müller, J Van Gent, H Eskes, Pieternel Felicitas Levelt, R Van Der A, JP Veefkind, J Vlietinck, et al. Impact of coronavirus outbreak on no2 pollution assessed using tropomi and omi observations. *Geophysical Research Letters*, 47(11):e2020GL087978, 2020.

Mingkui Cao, Stewart Marshall, and Keith Gregson. Global carbon exchange and methane emissions from natural wetlands: Application of a process-based model. *Journal of Geophysical Research: Atmospheres*, 101(D9):14399–14414, 1996.

Liang-Chieh Chen, George Papandreou, Iasonas Kokkinos, Kevin Murphy, and Alan L Yuille. Deeplab: Semantic image segmentation with deep convolutional nets, atrous convolution, and fully connected crfs. *IEEE transactions on pattern analysis and machine intelligence*, 40(4):834–848, 2017a.

Liang-Chieh Chen, George Papandreou, Florian Schroff, and Hartwig Adam. Rethinking atrous convolution for semantic image segmentation. *arXiv preprint arXiv:1706.05587*, 2017b.

Özgün Çiçek, Ahmed Abdulkadir, Soeren S Lienkamp, Thomas Brox, and Olaf Ronneberger. 3d u-net: learning dense volumetric segmentation from sparse annotation. In *Medical Image Computing and Computer-Assisted Intervention–MICCAI 2016: 19th International Conference, Athens, Greece, October 17-21, 2016, Proceedings, Part II 19*, pages 424–432. Springer, 2016.

Matthew J Cooper, Randall V Martin, Melanie S Hammer, Pieternel F Levelt, Pepijn Veefkind, Lok N Lamsal, Nickolay A Krotkov, Jeffrey R Brook, and Chris A McLinden. Global fine-scale changes in ambient no2 during covid-19 lockdowns. *Nature*, 601(7893):380–387, 2022.

Ivan Csiszar, Wilfrid Schroeder, Louis Giglio, Evan Ellicott, Krishna P Vadrevu, Christopher O Justice, and Brad Wind. Active fires from the suomi npp visible infrared imaging radiometer suite: Product status and first evaluation results. *Journal of Geophysical Research: Atmospheres*, 119(2):803–816, 2014.

Alessandro Damiani, Hitoshi Irie, Dmitry A Belikov, Shuei Kaizuka, Hossain Mohammed Syedul Hoque, and Raul R Cordero. Peculiar covid-19 effects in the greater tokyo area revealed by spatiotemporal variabilities of tropospheric gases and light-absorbing aerosols. *Atmospheric Chemistry and Physics*, 22 (18):12705–12726, 2022.

Bohdan Danylyshyn. The peculiarities of economic crisis due to covid-19 pandemic in a developing country: case of ukraine. *Problems and Perspectives in Management*, 18(2):13–22, 2020.

André de Palma, Shaghayegh Vosough, and Feixiong Liao. An overview of effects of covid-19 on mobility and lifestyle: 18 months since the outbreak. *Transportation Research Part A: Policy and Practice*, 159:372–397, 2022.

Carmelia Mariana Dragomir, Daniel-Eduard Constantin, Mirela Voiculescu, Lucian Puiu Georgescu, Alexis Merlaud, and Michel Van Roozendael. Modeling results of atmospheric dispersion of no2 in an urban area using meti–lis and comparison with coincident mobile doas measurements. *Atmospheric Pollution Research*, 6(3):503–510, 2015.

V. Dumitru, P. Inga, M. Danu, S. Andreas, K. Ievgen, and Y Viktoriia. Covid-19 impact on air quality in ukraine and the republic of moldova, 2020. URL `https://www.undp.org/ukraine/publications/covid-19-impact-air-quality-ukraine-and-republic-moldova`.

Bryan N Duncan, Yasuko Yoshida, Jennifer R Olson, Sanford Sillman, Randall V Martin, Lok Lamsal, Yongtao Hu, Kenneth E Pickering, Christian Retscher, Dale J Allen, et al. Application of omi observations to a space-based indicator of nox and voc controls on surface ozone formation. *Atmospheric Environment*, 44(18):2213–2223, 2010.

Liang Feng, Paul I Palmer, Robert J Parker, Mark F Lunt, and Hartmut Bösch. Methane emissions are predominantly responsible for record-breaking atmospheric methane growth rates in 2020 and 2021. *Atmospheric Chemistry and Physics*, 23(8):4863–4880, 2023.

Jerome H Friedman. Greedy function approximation: a gradient boosting machine. *Annals of statistics*, pages 1189–1232, 2001.

Pall Oskar Gislason, Jon Atli Benediktsson, and Johannes R Sveinsson. Random forests for land cover classification. *Pattern recognition letters*, 27(4):294–300, 2006.

Noel Gorelick, Matt Hancher, Mike Dixon, Simon Ilyushchenko, David Thau, and Rebecca Moore. Google earth engine: Planetary-scale geospatial analysis for everyone. *Remote sensing of Environment*, 202:18–27, 2017.

Stuart K Grange and David C Carslaw. Using meteorological normalisation to detect interventions in air quality time series. *Science of the Total Environment*, 653:578–588, 2019.

Stuart K Grange, David C Carslaw, Alastair C Lewis, Eirini Boleti, and Christoph Hueglin. Random forest meteorological normalisation models for swiss pm 10 trend analysis. *Atmospheric Chemistry and Physics*, 18(9):6223–6239, 2018.

Stuart K Grange, James D Lee, Will S Drysdale, Alastair C Lewis, Christoph Hueglin, Lukas Emmenegger, and David C Carslaw. Covid-19 lockdowns high-light a risk of increasing ozone pollution in european urban areas. *Atmospheric Chemistry and Physics*, 21(5):4169–4185, 2021.

Ghassan B Hamra, Francine Laden, Aaron J Cohen, Ole Raaschou-Nielsen, Michael Brauer, and Dana Loomis. Lung cancer and exposure to nitrogen dioxide and traffic: a systematic review and meta-analysis. *Environmental health perspectives*, 123(11):1107–1112, 2015.

Hans Hersbach, Bill Bell, Paul Berrisford, Gionata Biavati, András Horányi, Joaquín Muñoz Sabater, Julien Nicolas, Carole Peubey, Raluca Radu, Iryna Rozum, et al. Era5 hourly data on single levels from 1979 to present. *Copernicus climate change service (c3s) climate data store (cds)*, 10(10.24381), 2018.

Hitoshi Irie, Daichi Yonekawa, Alessandro Damiani, Hossain Mohammed Syedul Hoque, Kengo Sudo, and Syuichi Itahashi. Continuous multi-component max-doas observations for the planetary boundary layer ozone variation analysis at chiba and tsukuba, japan, from 2013 to 2019. *Progress in Earth and Planetary Science*, 8(1):31, 2021.

Syuichi Itahashi, Yuki Yamamura, Zhe Wang, and Itsushi Uno. Returning long-range pm2. 5 transport into the leeward of east asia in 2021 after chinese economic recovery from the covid-19 pandemic. *Scientific Reports*, 12(1):5539, 2022.

Akihiko Ito. Output data of greenhouse gas budget and carbon cycle simulated by the visit terrestrial ecosystem model, ver.2021.1_ch4wetl_cao, 2021a. URL `10.17595/20210521.001`.

Akihiko Ito. Output data of greenhouse gas budget and carbon cycle simulated by the visit terrestrial ecosystem model, ver.2021.1_ch4wetl_wh, 2021b. URL `10.17595/20210521.001`.

Akihiko Ito and Kazuhito Ichii. Terrestrial ecosystem model studies and their contributions to asiaflux. *Journal of Agricultural Meteorology*, 77(1):81–95, 2021.

Akihiko Ito, Yasunori Tohjima, Takuya Saito, Taku Umezawa, Tomohiro Hajima, Ryuichi Hirata, Makoto Saito, and Yukio Terao. Methane budget of east asia, 1990–2015: A bottom-up evaluation. *Science of the total environment*, 676: 40–52, 2019.

Xiaomeng Jin, Arlene Fiore, K Folkert Boersma, Isabelle De Smedt, and Lukas Valin. Inferring changes in summertime surface ozone–no x–voc chemistry over us urban areas from two decades of satellite and ground-based observations. *Environmental science & technology*, 54(11):6518–6529, 2020.

L. Júlia, M. Dylan, R. Danielle, and B Adrian. Nearly 3 million people have left ukraine, foreshadowing a massive humanitarian crisis, 2022. URL `https://www.washingtonpost.com/world/2022/02/27/ukraine-refugees-photos-videos/`.

Guolin Ke, Qi Meng, Thomas Finley, Taifeng Wang, Wei Chen, Weidong Ma, Qiwei Ye, and Tie-Yan Liu. Lightgbm: A highly efficient gradient boosting decision tree. *Advances in neural information processing systems*, 30, 2017.

Christine M Kendrick, Peter Koonce, and Linda A George. Diurnal and seasonal variations of no, no2 and pm2. 5 mass as a function of traffic volumes alongside an urban arterial. *Atmospheric Environment*, 122:133–141, 2015.

Laura Elena Cué La Rosa, Camile Sothe, Raul Queiroz Feitosa, Cláudia Maria de Almeida, Marcos Benedito Schimalski, and Dário Augusto Borges Oliveira. Multi-task fully convolutional network for tree species mapping in dense forests using small training hyperspectral data. *ISPRS Journal of Photogrammetry and Remote Sensing*, 179:35–49, 2021.

M. Lauri and G Rosa. Health impacts of coal power plant emissions in ukraine, 2021. URL `https://energyandcleanair.org/publication/health-impacts-of-coal-power-plant-emissions-in-ukraine/`.

Yiming Liu, Tao Wang, Trissevgeni Stavrakou, Nellie Elguindi, Thierno Doumbia, Claire Granier, Idir Bouarar, Benjamin Gaubert, and Guy P Brasseur. Diverse response of surface ozone to covid-19 lockdown in china. *Science of the Total Environment*, 789:147739, 2021.

Virginie Marécal, V-H Peuch, Camilla Andersson, Stefan Andersson, Joaquim Arteta, Matthias Beekmann, Anna Benedictow, Robert Bergström, Bertrand Bessagnet, Alberto Cansado, et al. A regional air quality forecasting system over europe: the macc-ii daily ensemble production. *Geoscientific Model Development*, 8(9):2777–2813, 2015.

Randall V Martin, Arlene M Fiore, and Aaron Van Donkelaar. Space-based diagnosis of surface ozone sensitivity to anthropogenic emissions. *Geophysical Research Letters*, 31(6), 2004.

Kazuyuki Miyazaki and Kevin Bowman. Predictability of fossil fuel co2 from air quality emissions. *Nature communications*, 14(1):1604, 2023.

Kazuyuki Miyazaki, Kevin Bowman, Takashi Sekiya, Masayuki Takigawa, Jessica L Neu, Kengo Sudo, Greg Osterman, and Henk Eskes. Global tropospheric ozone responses to reduced no x emissions linked to the covid-19 worldwide lockdowns. *Science Advances*, 7(24):eabf7460, 2021.

G. Nichita and M Ana. War in ukraine one year on, nowhere safe, 2023. URL `https://acleddata.com/2023/03/01/war-in-ukraine-one-year-on-nowhere-safe/`.

Carlos Ordóñez, Jose M Garrido-Perez, and Ricardo García-Herrera. Early spring near-surface ozone in europe during the covid-19 shutdown: Meteorological effects outweigh emission changes. *Science of the total environment*, 747:141322, 2020.

Shushi Peng, Xin Lin, Rona L Thompson, Yi Xi, Gang Liu, Didier Hauglustaine, Xin Lan, Benjamin Poulter, Michel Ramonet, Marielle Saunois, et al. Wetland emission and atmospheric sink changes explain methane growth in 2020. *Nature*, 612(7940):477–482, 2022.

Paulo Pereira, Wenwu Zhao, Lyudmyla Symochko, Miguel Inacio, Igor Bogunovic, and Damia Barcelo. The russian-ukrainian armed conflict impact will push back the sustainable development goals, 2022.

Hervé Petetin, Dene Bowdalo, Albert Soret, Marc Guevara, Oriol Jorba, Kim Serradell, and Carlos Pérez García-Pando. Meteorology-normalized impact of the covid-19 lockdown upon no 2 pollution in spain. *Atmospheric Chemistry and Physics*, 20(18):11119–11141, 2020.

Zhen Qu, Daniel J Jacob, Yuzhong Zhang, Lu Shen, Daniel J Varon, Xiao Lu, Tia Scarpelli, Anthony Bloom, John Worden, and Robert J Parker. Attribution of the 2020 surge in atmospheric methane by inverse analysis of gosat observations. *Environmental Research Letters*, 17(9):094003, 2022.

Clionadh Raleigh, rew Linke, Håvard Hegre, and Joakim Karlsen. Introducing acled: An armed conflict location and event dataset. *Journal of peace research*, 47(5):651–660, 2010.

Jie Ren, Fangfang Guo, and Shaodong Xie. Diagnosing ozone–no x–voc sensitivity and revealing causes of ozone increases in china based on 2013–2021 satellite retrievals. *Atmospheric Chemistry and Physics*, 22(22):15035–15047, 2022.

Caleb Robinson, Kolya Malkin, Nebojsa Jojic, Huijun Chen, Rongjun Qin, Changlin Xiao, Michael Schmitt, Pedram Ghamisi, Ronny Hänsch, and Naoto Yokoya. Global land-cover mapping with weak supervision: Outcome of the 2020 ieee grss data fusion contest. *IEEE Journal of Selected Topics in Applied Earth Observations and Remote Sensing*, 14:3185–3199, 2021.

Olaf Ronneberger, Philipp Fischer, and Thomas Brox. U-net: Convolutional networks for biomedical image segmentation. In *Medical Image Computing and Computer-Assisted Intervention–MICCAI 2015: 18th International Conference, Munich, Germany, October 5-9, 2015, Proceedings, Part III 18*, pages 234–241. Springer, 2015.

Mykhailo Savenets. Air pollution in ukraine: a view from the sentinel-5p satellite. *JOURNAL OF THE HUNGARIAN METEOROLOGICAL SERVICE*, 125(2): 271–290, 2021.

Felix Schiefer, Teja Kattenborn, Annett Frick, Julian Frey, Peter Schall, Barbara Koch, and Sebastian Schmidtlein. Mapping forest tree species in high resolution uav-based rgb-imagery by means of convolutional neural networks. *ISPRS Journal of Photogrammetry and Remote Sensing*, 170:205–215, 2020.

Quirin Schiermeier. Why pollution is falling in some cities—but not others. *Nature*, 580(7803):313, 2020.

Jason R Schroeder, James H Crawford, Alan Fried, James Walega, Andrew Weinheimer, Armin Wisthaler, Markus Müller, Tomas Mikoviny, Gao Chen, Michael Shook, et al. New insights into the column ch2o/no2 ratio as an indicator of near-surface ozone sensitivity. *Journal of Geophysical Research: Atmospheres*, 122(16):8885–8907, 2017.

Wilfrid Schroeder, Patricia Oliva, Louis Giglio, and Ivan A Csiszar. The new viirs 375 m active fire detection data product: Algorithm description and initial assessment. *Remote Sensing of Environment*, 143:85–96, 2014.

Andrii Shelestov, Hanna Yailymova, Bohdan Yailymov, and Nataliia Kussul. Air quality estimation in ukraine using sdg 11.6. 2 indicator assessment. *Remote Sensing*, 13(23):4769, 2021.

Zongbo Shi, Congbo Song, Bowen Liu, Gongda Lu, Jingsha Xu, Tuan Van Vu, Robert JR Elliott, Weijun Li, William J Bloss, and Roy M Harrison. Abrupt but smaller than expected changes in surface air quality attributable to covid-19 lockdowns. *Science advances*, 7(3):eabd6696, 2021.

Amir H Souri, Matthew S Johnson, Glenn M Wolfe, James H Crawford, Alan Fried, Armin Wisthaler, William H Brune, Donald R Blake, Andrew J Weinheimer, Tijl Verhoelst, et al. Characterization of errors in satellite-based hcho/no 2 tropospheric column ratios with respect to chemistry, column-to-pbl translation, spatial representation, and retrieval uncertainties. *Atmospheric Chemistry and Physics*, 23(3):1963–1986, 2023.

David S Stevenson, Richard G Derwent, Oliver Wild, and William J Collins. Covid-19 lockdown emission reductions have the potential to explain over half of the coincident increase in global atmospheric methane. *Atmospheric Chemistry and Physics*, 22(21):14243–14252, 2022.

T.F. Stocker, G.-K. Plattner D. Qin, M. Tignor, S.K. Allen, J. Boschung, A. Nauels, Y. Xia, V. Bex, and P.M. Midgley. Ipcc, 2013: Climate change 2013: The physical science basis. contribution of working group i to the fifth assessment report of the intergovernmental panel on climate changes. Technical report, Cambridge University Press, Cambridge, United Kingdom and New York, NY, USA, 2013.

Akira Tani and Tomoki MOCHIZUKI. Exchanges of volatile organic compounds between terrestrial ecosystems and the atmosphere. *Journal of Agricultural Meteorology*, 77(1):66–80, 2021.

Alexander J Turner, Christian Frankenberg, and Eric A Kort. Interpreting contemporary trends in atmospheric methane. *Proceedings of the National Academy of Sciences*, 116(8):2805–2813, 2019.

Jos Van Geffen, Henk Eskes, Steven Compernolle, Gaia Pinardi, Tijl Verhoelst, Jean-Christopher Lambert, Maarten Sneep, Mark Ter Linden, Antje Ludewig, K Folkert Boersma, et al. Sentinel-5p tropomi no 2 retrieval: impact of version v2. 2 improvements and comparisons with omi and ground-based data. *Atmospheric Measurement Techniques*, 15(7):2037–2060, 2022.

Julie Wallace and Pavlos Kanaroglou. The effect of temperature inversions on ground-level nitrogen dioxide (no2) and fine particulate matter (pm2. 5) using temperature profiles from the atmospheric infrared sounder (airs). *Science of the Total Environment*, 407(18):5085–5095, 2009.

Bernadette P Walter and Martin Heimann. A process-based, climate-sensitive model to derive methane emissions from natural wetlands: Application to five wetland sites, sensitivity to model parameters, and climate. *Global Biogeochemical Cycles*, 14(3):745–765, 2000.

Chi Wang, Qingyun Wu, Markus Weimer, and Erkang Zhu. Flaml: A fast and lightweight automl library. *Proceedings of Machine Learning and Systems*, 3: 434–447, 2021.

Rasa Zalakeviciute, Danilo Mejia, Hermel Alvarez, Xavier Bermeo, Santiago

Bonilla-Bedoya, Yves Rybarczyk, and Brian Lamb. War impact on air quality in ukraine. *Sustainability*, 14(21):13832, 2022.

Zhen Zhang, Benjamin Poulter, Andrew F Feldman, Qing Ying, Philippe Ciais, Shushi Peng, and Xin Li. Recent intensification of wetland methane feedback. *Nature Climate Change*, 13(5):430–433, 2023.

Maria A Zoran, Roxana S Savastru, Dan M Savastru, and Marina N Tautan. Peculiar weather patterns effects on air pollution and covid-19 spread in tokyo metropolis. *Environmental Research*, 228:115907, 2023.